# Quantitative inference of population response properties across eccentricity from motion-induced maps in macaque V1

**Malte J. Rasch, Ming Chen, Si Wu, Haidong D. Lu and Anna W. Roe**

*J Neurophysiol* 109:1233-1249, 2013. First published 28 November 2012;
doi: 10.1152/jn.00673.2012

*J Neurophysiol* 109: 1233–1249, 2013.
First published November 28, 2012; doi:10.1152/jn.00673.2012.

# Quantitative inference of population response properties across eccentricity from motion-induced maps in macaque V1

**Malte J. Rasch,[1,2] Ming Chen,[2] Si Wu,[1,2] Haidong D. Lu,[2] and Anna W. Roe[3]**

[1]*State Key Laboratory of Cognitive Neuroscience and Learning, Beijing Normal University, Beijing, China;* [2]*Institute for Neuroscience, State Key Laboratory of Neuroscience, Shanghai Institutes for Biological Sciences, Shanghai, China; and* [3]*Department of Psychology, Vanderbilt University, Nashville, Tennessee*

Submitted 3 August 2012; accepted in final form 27 November 2012

**Rasch MJ, Chen M, Wu S, Lu HD, Roe AW.** Quantitative inference of population response properties across eccentricity from motion-induced maps in macaque V1. *J Neurophysiol* 109: 1233–1249, 2013. First published November 28, 2012; doi:10.1152/jn.00673.2012.—Interpreting population responses in the primary visual cortex (V1) remains a challenge especially with the advent of techniques measuring activations of large cortical areas simultaneously with high precision. For successful interpretation, a quantitatively precise model prediction is of great importance. In this study, we investigate how accurate a spatiotemporal filter (STF) model predicts average response profiles to coherently drifting random dot motion obtained by optical imaging of intrinsic signals in V1 of anesthetized macaques. We establish that orientation difference maps, obtained by subtracting orthogonal axis-of-motion, invert with increasing drift speeds, consistent with the motion streak effect. Consistent with perception, the speed at which the map inverts (the critical speed) depends on cortical eccentricity and systematically increases from foveal to parafoveal. We report that critical speeds and response maps to drifting motion are excellently reproduced by the STF model. Our study thus suggests that the STF model is quantitatively accurate enough to be used as a first model of choice for interpreting responses obtained with intrinsic imaging methods in V1. We show further that this good quantitative correspondence opens the possibility to infer otherwise not easily accessible population receptive field properties from responses to complex stimuli, such as drifting random dot motions.

critical speed of inversion; receptive fields; motion response; optical imaging; primary visual cortex; spatiotemporal filtering model; eccentricity

MUCH OF OUR UNDERSTANDING about the function of primary visual cortex (V1) is centered on the concept of a receptive field (RF). Neurons of V1 have been classically described by a spatiotemporal filter (STF) model (Hubel and Wiesel 1962; Movshon et al. 1978; Adelson and Bergen 1985, Mante and Carandini 2005; Baker and Issa 2005). In this model, the shape of the filter can be identified as the RF of a neuron. The model assumes that the mean firing rate of a single (complex) neuron can be described as proportional to (the square of) a filtered version of the luminance information falling into its RF (the luminance "energy").

While this simple view has been challenged by the notion that the known anatomical complexity of V1 (such as diverse lateral and intercortical connections) might give rise to a multitude of extra-classical field properties in single neuron recordings (e.g., see Angelucci and Bressloff 2006), it is nevertheless commonly believed that the model at least approximately describes the time-averaged population responses as accessible with intrinsic optical imaging or functional MRI-related methods. For instance, recent studies investigating population responses using optical imaging showed that the STF model qualitatively captures the average population responses in the primary visual area in ferrets and cats (Baker and Issa 2005; Basole et al. 2003; Mante and Carandini 2005; Zhang et al. 2007). However, since neither study directly compared model predictions with experimentally obtained data for multiple cortical sites and across orientation domains, it is still unclear (especially in macaques) to what degree the STF model indeed predicts average population responses in a quantitative manner. Such examination is needed to establish the generality of the STF model across cortical sites and across functional domains.

If the STF model would predict the population responses measured with optical imaging techniques in a quantitative sense for relatively simple stimuli, it could be used as a general "null hypothesis model" for contrasting observed responses to very complex stimuli. For instance, the STF model might be too simplistic to predict responses to some illusory patterns, but unknown nonlinear contributions in the observed activations are difficult to dissect from the "trivial" response without a quantitative model for the latter at hand.

Furthermore, if the STF model was even numerically accurate for intermediate complex stimulus conditions, it could also be applied to infer RF properties using these stimulus conditions, such as motion-induced activations of random dot patterns or noise patterns having naturalistic frequency spectrum. Constraining the model to fit such optical imaging measurements would yield estimates of RF properties of the underlying neural populations (because RF variables are parameters of the model) that might be otherwise not easily accessible. This approach would be particularly effective if the model prediction can still be calculated with analytical formulas. Importantly, this approach would estimate population RF parameters without relying on presenting artificial grating stimuli that might drive the visual system into a nonnatural regime.

In this study, we make a first step towards establishing the accurateness of the STF model under a set of motion stimulus conditions in monkeys to open the way for a wider application of the STF model to imaging data.

Here we investigate a case of motion-induced activation in V1 in macaque monkeys. We present coherently drifting random-positioned luminance dots while recording neural responses using intrinsic optical imaging. We establish that

Address for reprint requests and other correspondence: M. J. Rasch, State Key Laboratory of Cognitive Neuroscience and Learning, Beijing Normal Univ., 19 Xinjiekouwai St., Beijing 100875, China (e-mail: malte@bnu.edu.cn).

motion-induced orientation maps can be observed in V1 of macaques. This motion-induced neural activation is caused by so-called "motion streaks" or "speed lines" (Geisler 1999; Burr and Ross 2002; Geisler et al. 2001) referring to a perceived line in the direction of the movement if, e.g., a small light point moves very fast across the visual field. This phenomenon is commonly experienced when observing fireworks and is smartly exploited by comic strip artists to indicate rapid movements. We further show that when changing the velocity of the drift of the random dot pattern, the peak activation abruptly shifts from perpendicular to parallel to the movement direction, so that observed orientation maps "invert" at a critical speed, consistent with the motion streak effect and predicted by earlier theoretical studies (Mante and Carandini 2005; Baker and Issa 2005). Careful measurements reveal that the critical speed changes gradually with cortical position forming a "critical speed map" in V1.

To test the accurateness of the STF model using this motion streak paradigm, we derive formulas for the predicted response profiles to moving random dots as well as for the critical speed and compared predictions with observations. Taking into consideration the known variability between animals, we found that critical speeds and response profiles across orientation domains and eccentricities are surprisingly well predicted by the STF model. These good model predictions suggest that the STF model is well suited to quantitatively describe population responses measured with hemodynamic signals in primary visual cortex and should thus serve as a first model of choice to interpret activations to complex stimuli. We further show that the STF model can be successfully used to infer population RF properties from the response profiles to motion-induced random dots.

Some of the experimental observations have previously been reported in abstract form (Lu et al. 2007).

## MATERIALS AND METHODS

### *Experimental Methods*

*Recording setup.* For a detailed description of the recording setup see Roe and Ts'o (1995), Lu and Roe (2007), and Lu et al. (2010). Briefly, data were collected from six macaque monkeys (abbreviated with *M1–M6*; *M1*, *M2*, *M6*: *Macaca mulatta*; *M3–M5*: *Macaca fascicularis*) in anesthetized and paralyzed conditions. All procedures were in accordance with the U.S. National Institutes of Health Guidelines and were approved by the Institutional Animal Care and Use Committees (Institute of Neuroscience, Chinese Academy of Sciences; Vanderbilt University). Monkeys were anesthetized (thiopental sodium, 1-2 $mg \cdot kg^{-1} \cdot h^{-1}$ iv and isoflurane, 0.2–1.5%), paralyzed with vecuronium bromide (0.05 $mg \cdot kg^{-1} \cdot h^{-1}$ iv), and artificially ventilated. Anesthetic depth was assessed continuously via implanted wire electroencephalographic electrodes, end-tidal $CO_2$, oximetry, and heart rate. A craniotomy and durotomy were performed to expose visual areas V1 and V2 (near the lunate sulcus). In *monkeys M2* and *M3*, a chronic chamber (diameter 22 mm) was implanted. In *monkeys M1* and *M4–M6*, data were collected before the chamber implant. In chamber imaging experiments, an artificial dura (Chen et al. 2002) was used to protect the cortex and also help with cortical stabilization. Eyes were dilated (atropine sulfate) and fit with contact lenses of appropriate curvature to focus on a computer screen 57 cm from the eyes. Eyes were plotted using a rapid retinotopic imaging method (Lu et al. 2009). The brain was stabilized with agar, and images were obtained through a cover glass. Images of reflectance change (intrinsic hemodynamic signals) corresponding to local cortical activity were acquired with 632-nm illumination. Frame size was 504 × 504 pixels and represented a square of 10–20 mm depending on the monkey and on the imaging lens used. All stimuli were presented in a randomly interleaved fashion and were presented in blocks. Each block contained sets of stimuli consisting of either full-field gratings of different drifting directions with optimized spatial (SFs) and temporal frequencies (TFs; see Lu and Roe 2007) or four random dot patterns (drifting in one of four directions: 0, 90, 180, and 270) and a blank. Visual stimuli were created using ViSaGe (Cambridge Research Systems, Rochester, UK) and presented on a gamma corrected CRT monitor (SONY GDM F500R or CPD-G520). Mean luminance for all stimuli, including the blank stimulus, was kept at 30 $cd/m^2$. Random dot patterns consisted of white dots (2 × 2 pixels, corresponding to a side length of 0.128° for *M1* and 0.116° for *M3–M5*), presented at a density that covered 3% of the monitor area (4% in *M1*), and drifted at various speeds (as described below). Each stimulus was presented for 3.5 s after a 0.5-s blank screen, during which 16 consecutive frames were imaged. Interstimulus interval for all stimuli was at least 8 s. After recording, data were processed by custom written MATLAB scripts (Version R2011a; MathWorks, Natick, MA).

*Data analysis.* We performed three types of experiments as described in RESULTS. In *experiment 1*, random dots stimuli drifting with six different speeds (1, 2, 4, 8, 16, and 32°/s) were presented to *monkey M1* (35 trials). After recording, raw signals were averaged and neural signals were obtained by subtracting the mean of time frames 1 and 2 from 14 to 16. To reduce the blood vessel noise, signals were normalized by the power of the second Fourier component along the time frames (after averaging over all conditions). This normalization reduced artifacts and resulted in (visually) superior orientation maps than for more conventional methods. Subsequently, signals were filtered using a (2D) Butterworth filter (high-pass, 0.4 cycles/mm, order 4; and low-pass, 5 cycles/mm, order 1). In an analogous manner, an orientation map was generated based on a separate run using gratings (10 trials, 4 orientations). Blood vessels and noncortical regions were excluded by thresholding the described normalization term and the trial-to-trial variance (thresholds adjusted manually). Additionally, not robustly activated pixels during the orientation map recordings were excluded (*t*-test allowing for different variances, threshold set manually).

To generate difference maps of the axis-of-motion, trials from the two opposing directions were averaged and orthogonal directions were subtracted. Since the spatial luminance distribution of the random dot pattern was isotropic, the differential activation of the orientation domains could only be caused by the drifting motion. Average response profiles were obtained by sorting each pixel of a region of interest (ROI) into one of 25 bins according to the orientations established by the reference orientation map and averaged. Error bars report the SE, corrected for the correlation induced by the low-pass filtering. For the low-pass used here, the expected correlation is four pixels. Thus we divided the number of averaged pixels in the SE calculation by $4^2\pi$.

In *experiment 2*, three monkeys (*M3–M5*) were presented with random dot stimuli with 31–41 densely spaced drifting speeds in the interval 2 to 10°/s (2 to 8 in *M4*). Each stimulus was repeated two to eight times, and the direction of coherent dot motion (4 directions) was randomized (in *monkey M5*, also speeds were randomized over the whole experimental time). To minimize any potential chamber shift during the long experiments, frames were realigned in respect to the orientation map by maximizing the correlation of the central part. The orientation map was obtained in a separate run (8 full-field grating orientations). Raw data were processed on a single trial basis, since response profiles could be obtained reliably even for single trials. Here, neural signals were extracted by directly using the negative logarithm of the power of the second Fourier component along the recorded time frames yielding superior artifact reduction on single trial basis than traditional methods. Average response profiles were obtained as above (except using low pass of 8.33 cycles/mm).

The critical speed was estimated by first re-binning the difference activation maps using two bins (centered at 0 or 90°, respectively). After all values falling in either of the bins were collected, *t*-test statistics allowing for different sample variances were computed for all speeds. Zero crossing of the t-values indicated the critical speed (linearly fitted in the range of 2 to 6°/s). The confidence interval (CI) of the critical speed was based on the 95% CI of the linear fit.

In *experiment 3*, the goal was to estimate RF parameters with traditional spatiotemporal gratings. Two monkeys (*M2* and *M6*) were shown 25 gratings (1 orientation; 20 trials) of various SFs (0.3, 0.6, 1.2, 2.4, and 4.8 cycles/°) and TFs (1, 2, 4, 8, and 16 Hz and 0.25, 0.75, 2.25, 6.75, and 20.25 Hz, respectively). Additionally in a third monkey (*M4*), six gratings were shown (SF: 0.3, 0.6, 1.2, 2.4, 4.8, 9.6 cycles/°; TF: 8 Hz). All data were processed as in *experiment 2*. Response profiles were constructed by averaging the activation according to a reference orientation maps (single condition map, blank subtracted). Orientation maps were recorded in separate runs (4 orientations). Fitting was achieved by minimizing the mismatch of the STF model responses (see APPENDIX) and the measured responses (direct simplex method with random initial conditions). Pearson correlation over all 50 (concatenated) response profiles simultaneously was used as goodness-of-fit measure. Minimal responses were set to zero to adjust offsets from the baseline, and the symmetrical profiles were averaged to half-profiles before the fit. To ensure physiological reasonable RFs, we enforced physiological bounds on the RF parameters (SF and TF preferences 0.1–20 cycles/°, band widths from 0.1 to 10 octaves, and aspect ratio from 1 to 2; see APPENDIX for definitions of the parameters). Convergence was robust, and the best match was usually obtained for most of the randomly chosen initial conditions.

### *STF Model*

The orientation response to a spatially isotropic but constantly and coherently moving random dot pattern can be understood when modeling the average activity of neurons in the primary visual cortex by a STF mechanism (Baker and Issa 2005; Geisler 1999; Mante and Carandini 2005). Explaining the V1 responses by a filter mechanism is the classical approach to V1 and has been suggested decades ago (Adelson and Bergen 1985; Hubel and Wiesel 1962; Movshon et al. 1978; Watson and Ahumada 1985). We call this model the STF model. In the APPENDIX, we use such a filtering model based on the classical assumptions of Gabor RFs (Jones and Palmer 1987) and the energy mechanism in complex cells (Adelson and Bergen 1985) to derive analytic equations for calculation of the expected critical speed and for the predicted neural responses to random dot stimuli as used in the experiments.

The STF model is a feed-forward input-driven model of average responses in the early visual cortex. We derive the model in mathematical detail in the APPENDIX. Briefly, neural responses are treated as proportional to a filtered version of a given spatiotemporal input stream (i.e., temporally changing luminance intensities in the visual field). Each neural site thus implements a STF that we think of as the RF of a small population of neurons (and subsequently call it an RF filter or simply RF). This filter is tuned to features in the input stream, namely orientation, TF, SF, and visual field position. Since we are interested in the average response and the moving random dot stimulus is (on average) identical for each visual position, all potential visual field positions or temporal offsets can be averaged, so that only one mean response value remains for each orientation domain, cortical region, and stimulus presentation.

Using this STF model, we derive formulas to predict the critical speed of inversion for drifting random dots and white noise stimuli (see *Eqs. 1* and *2*).

## RESULTS

We investigate motion-induced activation in V1 across several degree eccentricity in macaque monkeys and evaluated the accurateness of the STF model prediction. We presented coherently drifting, randomly positioned luminance dots while recording neural responses using intrinsic optical imaging.

Altogether six macaque monkeys (*M1–M6*) participated in the experiments in an anesthetized condition.

### *Orientation Maps Invert for Increasing Drifting Speeds in Macaque*

We first established whether motion-induced orientation maps can be observed in V1 of macaques and investigated how different velocities affect these maps. Figure 1*B* illustrates the characteristic pattern of orientation domains obtained in macaque V1 in response to oriented drifting gratings (*monkey M1*, approximate V1 region of interest indicated); we refer to this map as the reference orientation map. We then presented stimuli composed of randomly positioned luminance dots drifting in one of four directions (up, down, left, or, right) and at one of six drift speeds. To obtain motion-induced orientation maps, imaged trials were averaged, oppositely drifting directions summed, and orthogonal motion axes subtracted (illustrated in Fig. 1*C*). These axis-of-motion maps obtained at drift speeds of 1, 2, 4, 8, 16, and 32°/s are shown in Fig. 1*D*.

These maps reveal clear differential activation to orthogonal motion axes. As shown in Fig. 1*E* (2 enlarged ROI in V1: blue and orange), the whole V1 region spanning several degrees eccentricities exhibits regular arrays of axis-of-motion domains similar to the orientation domains obtained with drifting gratings. To quantify the axis-of-motion response, for each map, we averaged the activation of all pixels with matching orientation preference (defined by the reference orientation map). In detail, after computing a preferred orientation for each pixel according to the relative responses to the four grating orientations (i.e., calculating the circular mean for each pixel), we binned these orientation preferences into 25 bins from 0 to 180° and determined the orientation bin each pixel belonged to. We then averaged all corresponding pixel locations in the axis-of-motion map belonging to the same orientation bin in the reference map. This resulted in the axis-of-motion difference response profiles shown in Fig. 1*F* (blue curve; averaged over the whole V1 ROI). Similar to previous profiles obtained for grating-derived orientation maps (e.g., Lu et al. 2010), profiles peak at a particular orientation and gradually fall off for intermediate orientations, illustrating the differential activation by orthogonal drift axes.

Importantly, in agreement with the motion streak effect, maps were observed to invert when drift speeds increased from low to high. As seen in Fig. 1*F*, profiles peaked at zero degree for speeds up to ~4°/s and inverted (to 90°) for speeds >8°/s. We refer to the speed at which the orientation map inverts, as the critical speed. The inversion was evident not only in pixel averages across the imaged cortex but also on a pixel-by-pixel basis. This can be observed by examining individual domains outlined in the difference maps in Fig. 1*E* (arrows). For increasing drifting speeds, individual pixels inverted in contrast, reflecting a change in the axis-of-motion response preference. In addition, the magnitudes of response preference changed with drift speed. In this example, drift speed at 16°/s

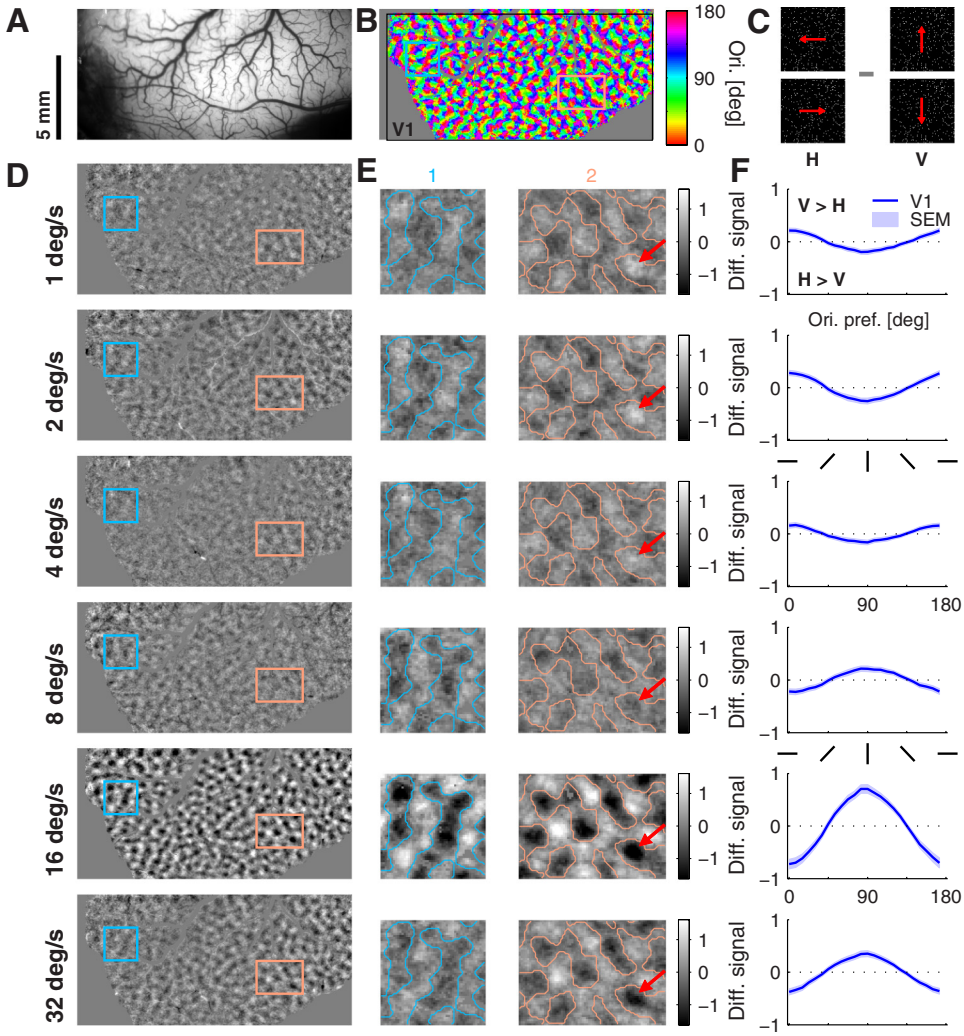


Fig. 1. Optical imaging measurements in response to coherently drifting dots in monkey M1. *A*: blood vessel map of the exposed visual cortex. *B*: reference orientation map obtained with grating stimuli. *C*: stimulus used in experiments. Opposite directions are pooled to generate axis-of-motion difference map. *D*: axis-of-motion difference maps to 6 drifting speeds. Orientation domains are differentially activated resulting in typical patchy patterns across the cortex. *E*: magnified regions as marked in *D*. Contour lines indicate oblique orientation domains. Note that pixels invert contrast for increasing speed (for example, the region indicated by arrows). *F*: averaged difference response profiles [regions of interest (ROIs) indicated in *B*]. Profiles are normalized by a constant factor for better visualization. Shaded areas mark SE. Note that neural activation and optical signals are anticorrelated: orientation domains stronger activated by vertical motion (V) show positive signals, domains that are stronger activated by horizontal motion (H) show negative signals (as indicated in the plots).

produced the strongest maps. Thus each drift speed produced a characteristic difference profile (Fig. 1*F*).

### *Determining the Critical Speed of Inversion at Different Eccentricities*

Having established that orientation maps invert with speed, we aimed to determine the value of the critical speed more accurately and to examine whether this speed changes with eccentricity. To more accurately estimate the critical speed, in three macaques (*M3–M5*), drift speeds of random dot patterns were varied in finer steps (31–41 different speeds) in the range of 2 to 10°/s. We then conducted retinotopic mapping of the imaged region using concentric rings and bars of known eccentricity and fitted activations with cortical magnification functions to obtain pixel-based estimates of retinotopic eccentricity (see Fig. 2).

We then determined inversion speeds in the following manner, illustrated for *monkey M3* in Fig. 3. After obtaining the reference orientation map (Fig. 3*C*), we obtained axis-of-motion maps and, for each speed, difference response profiles as before. Observed difference response profiles for *monkey M3* are shown color-coded in Fig. 3*A* (for this example, the ROI is indicated in Fig. 3*C*: V1 responses were pooled for pixels between 2 and 3° eccentricity only). As in Fig. 1, response profiles showed an inversion for increasing speed; however, because of the fine spacing between tested speeds, the critical speed could be estimated with greater precision. Figure 3*B* illustrates the estimate of inversion speed. We used *t*-values allowing for dissimilar variances to compare whether the activation of the horizontal and vertical axis-of-motion domains differ (see Fig. 3*B* and MATERIALS AND METHODS for details). *T*-values are plotted in Fig. 3*B* for multiple drifting speeds. Since the difference activation to horizontal and vertical motion will change sign when the profiles inverts, we estimated the critical speed at the zero crossing of a linear fit (line in Fig. 3*B*). The estimated critical speeds in V1 for each monkey and different eccentricities are summarized in Fig. 4*A*. Critical speeds fell between 2–5°/s depending on the monkey and eccentricity. In V1 (in the range of 2–3° eccentricity) of *monkeys M3* and *M5*, the critical speed was 4.12°/s (CI: 4.11···4.13°/s; CI calculation based on the 95% CI of the linear fit) and 3.19°/s (2.7···3.4°/s), respectively.

One monkey (*M4*) showed almost 2°/s lower critical speeds than the other monkeys. In fact, its critical speed was too low to be reliably estimated in the 2–3° eccentricity region in our data (critical speeds for larger eccentricities could be estimated, see Fig. 4*A*). In contrast to *M4*, all other monkeys exhibited critical speeds consistently at ~4°/s. This discrepancy might be caused by an exceptional low preferred TF in

*monkey M4* and data from this monkey were therefore excluded from some of the further analysis of the critical speed (see DISCUSSION).

To examine whether the critical speed changes with eccentricity, we divided V1 into regions from lower to higher eccentricity [in steps of 0.3–0.5° using rectangular boundaries in the case of *monkeys M3* and *M5* (as indicated in Fig. 3*D* for *M3*), and using nonrectangular regions based on a 2D eccentricity map for *M4*] and calculated the critical speed on the pooled responses within each region (Fig. 4*A*). Critical speeds in the V1 subregions of individual monkeys were less variable (within 1°/s) than between monkeys. Interestingly, for individual monkeys, the critical speed systematically increased with greater visual field eccentricity [testing for linear trend, $F = 207$, 55, and 63 for *M3–M5*; $P < 0.001$. If (uniform) random values from each CI are taken instead, 95% quantile of all $P$ values (1,000 repeats): 0.0003, 0.0418, and 0.0305]. In one monkey (*M3*), data were sufficient to generate a critical speed map over all measured cortical positions (Fig. 3*D*). Here, critical speed was estimated on individual pixel basis by calculating the trial-averaged difference activation between horizontal and vertical directions of movement and identifying the speed where the difference activation crossed zero (after smoothing). This color-coded critical speed map illustrates the gradual increase in critical speed from lateral (central) to medial (peripheral) V1 and demonstrates the eccentricity dependence of the motion streak effect.

According to the model equations (see APPENDIX), the predicted response profiles to drifting dots and the critical speed depend crucially on the RF properties of the underlying neural population. The observed change of the critical speed with eccentricity is thus likely a result of the change in the neural RF properties with eccentricity. To directly measure the change of SF preference with eccentricity, we showed gratings of fixed TF (8 Hz) but varying SFs (0.3–9.6 cycles/°) in one monkey (*M4*) as a control experiment. As expected, the SF preference decreased markedly from ~4.5 cycles/° (at 1.5° eccentricity) to 1.4 cycles/° (at 5.5° eccentricity; see Fig. 4*B* black crosses). Note that the abrupt jump in the SF preference estimation for eccentricities around 3.5° might be related to limited amount of data in this control experiment.

### *Theoretical Calculation of the Critical Speed*

The change of the peak response from parallel to perpendicular orientation domains in the "motion streak" paradigm is qualitatively well understood by the STF model (see Fig. 5*A*; see APPENDIX for mathematical derivations). If dot motion is slow, the band-pass filter of the RF acts as a temporal high-pass filter and edges of the dots (perpendicular to the movement direction, Fig. 5*C*) are the most striking feature activating perpendicular domains; if the dot motion is fast, the band-pass acts as temporal low-pass filter, integrating luminance along the path of movement (Fig. 5*D*) and activating mostly parallel orientation domains instead. Thus a change of the relative contribution of parallel and perpendicular orientation domains is expected when increasing the drifting speeds from slow to fast. The speed at which the

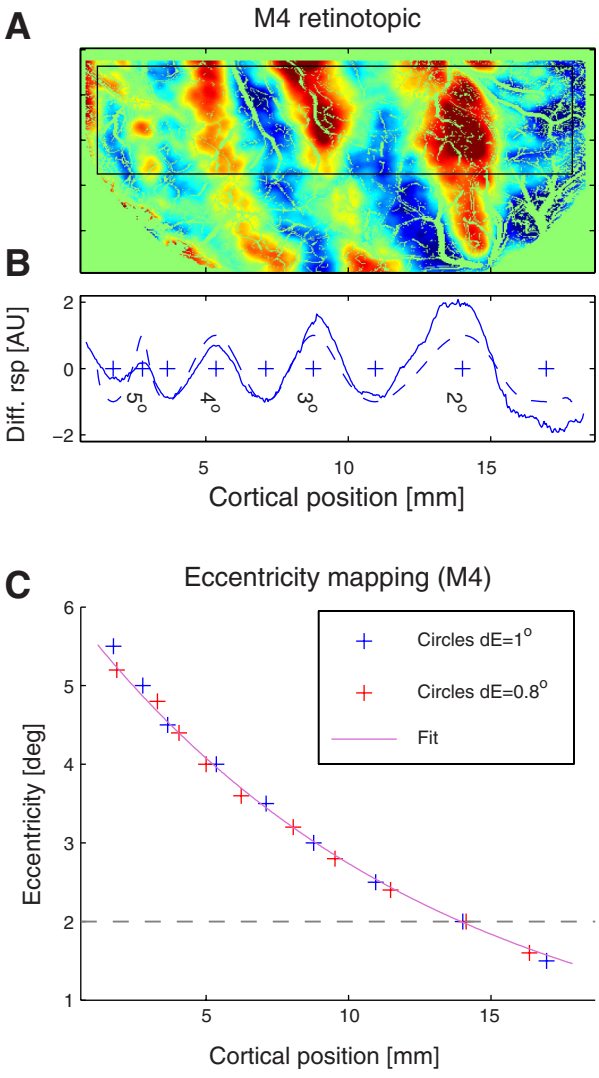


Fig. 2. Determining retinotopic map in imaged field of view. To approximate the eccentricity range of each pixel, in one monkey (*M4*), we showed concentric circles. Since the circles had constant and known eccentricity, the cortical positions of reference eccentricities could be inferred from the peak activation in this experiment. *A*: difference image of concentric rings (1, 2, 3, 4, 5, and 6° vs. 0.5, 1.5, 2.5, 3.5, 4,5, and 5.5° radius). Activation is smoothed and trial-averaged. *B*: peak activations yield eccentricity estimate (from the vertical average of black box in *A*). Dashed lines: constant amplitude signal from Hilbert transform. *C*: since the inverse cortical magnification factor (CMF) is linearly related with eccentricity (Schwartz 1980; Tootell et al. 1988), the relation of eccentricity to cortical position can be very well fitted. Peak positions fitted with $E(x) = a/b\{\exp[b(x + c)] - 1\}$, ($x$: relative cortical position), the equation reflecting linear relationship between inverse CMF and eccentricity ($E$): $CMF^{-1} = a + bE$. The fit resulted in $a = 6.31 \times 10^{-5}$ °/mm, $b = 0.08$ mm$^{-1}$, and $c = 98$ mm. The relation is here replotted in cortical position as in *A* and *B*. Blue crosses are from data in *A* and *B*, red crosses from an additional experiment with a different set of ring radii (1.2, 2, 2.8, 3.6, 4.4, 5.2, and 6° vs. 0.8, 1.6, 2.4, 3.2, 4, 4.8, and 5.6° radius). Reference position was set to the cortical position at 2° (dashed-dotted line in *C*), where activation to both sets of radii coincided. In all other experimental sessions, vertical and horizontal bars of fixed positions were shown instead (cf. Lu et al. 2010; Fig. 1*D*). Cortical distance between activation to two bars near and parallel to the V1/V2 border was used to estimate the absolute eccentricities in the imaged field of view according to the fitted equation above. Since parallel bars do not produce concentric cortical activations, we did not determine a full 2D eccentricity map in monkeys other than *M4*. Instead, since we found from *M4* that eccentricity is approximately constant perpendicular to the V1/V2 border in a region within ~5 mm cortex (as indicated in the rectangular area in *A*), we only considered pixels nearer than 5 mm from the V1/V2 border in *M3* and *M5* when defining rectangular ROIs based on eccentricity (see RESULTS). Eccentricity at the V1/V2 border should yield a good estimate throughout these small regions. AU: arbitrary units.

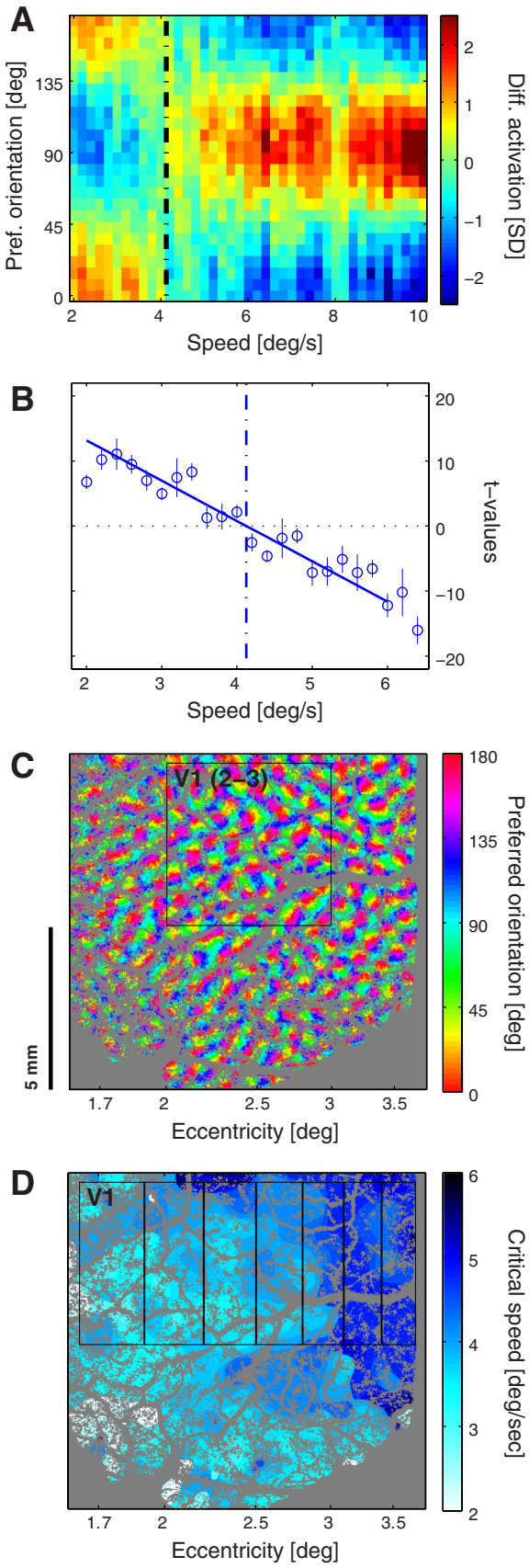


perpendicular domains respond with equal strength as the parallel domains, we call the critical speed.

Intuitively, expected responses to drifting dot motion are very accessible when seen in the frequency domain. The STF model can be understood by imagining the RFs as localized regions in frequency space that integrate the energy of the stimulus falling into the volume of the RF (Baker and Issa 2005; Mante and Carandini 2005). As derived in the APPENDIX and illustrated in Fig. 5*E*, the energy of a coherently drifting luminance pattern is arranged on a tilted plane (and having an approximate Gaussian shape on this plane in case of random dots), where the tilt angle is directly related to the speed of motion. If the drifting speed is low (small tilt angle), the tilted plane will intersect mostly with the perpendicular domain (red blobs in Fig. 5*E*), whereas if the speed is high the plane will instead reach the parallel orientation domain (green blobs in Fig. 5*E*) without intersecting the perpendicular domain significantly. Since the activation level is proportional to the amount of energy in the intersection, the relative contribution of perpendicular and parallel domains will thus change when drifting speeds are varied. The drifting speed at which both contributions are equal is the critical speed.

Our formulation of the STF model is fully characterized by six parameters (see Fig. 6). Namely, the orientation, SF and TF preferences and the three respective bandwidths, defining the tuning widths to each of the three features. Assuming that at the critical speed the activations to drifting random dots of perpendicular and parallel orientation domains are equal, we derived an approximate formula for the critical speed $\mu_{RD}$. We found that (see the APPENDIX for a derivation):

$$\mu_{RD} = \omega\left(\frac{d_\rho}{d_\omega \rho} + \frac{\rho'}{\alpha d_\omega}\right) \frac{d_\omega d_\rho \pm \sqrt{d_\rho^2\left(d_\omega^2 - \log 2\right) - \left(1+\rho'^2\right)\log^2 2}}{d_\rho^2 + \left(1+\rho'^2\right)\log 2} \quad (1)$$

The expression involves the parameters of the model, a parameter signifying the size of the dots ($\alpha$) and uses the abbreviation $\rho' \equiv \rho/(d_\rho \alpha)$ (see APPENDIX for an explanation of the parameters). Further theoretical analysis of *Eq. 1* shows that the critical speed crucially depends on the "preferred speed" of the neural population. The preferred speed is defined as the ratio of the preferred TF $\omega$ to preferred SF $\rho$ and is given in degress per second. In particular, we found that Equation 1 reduces to the case of drifting white noise luminance patterns if the size of the dots is small enough (compared to the SF selectivity of the neural population).

Fig. 3. Measuring the critical speed using drifting random dots of finely spaced drifting speeds in monkey *M3*. *A*: average orientation difference profiles in color code for V1. Difference responses are normalized to the sample SD calculated on the whole data set. Note that the response peak shifts from 0 to 90° at 4.1°/s (V1). Dashed lines: estimated critical speed from *B*. V1 data were pooled from regions of interest as indicated in *C*. *B*: normalized difference between the average activation of horizontal and vertical domains (*t*-values); crossing the zero line means inversion of the difference map and provides critical speed (linear fit in the interval 2 to 6°/s). *C*: reference orientation map obtained in a separate run using full-field gratings. Region of interest of *A* and *B* is indicated by a rectangle. Data in V1 are only taken from pixels having eccentricities between 2 and 3° as for the model prediction (Fig. 7). *D*: critical speed map. Critical speed increases with eccentricity. Regions of interest used in Fig. 4 (red triangles) are indicated (black rectangles).

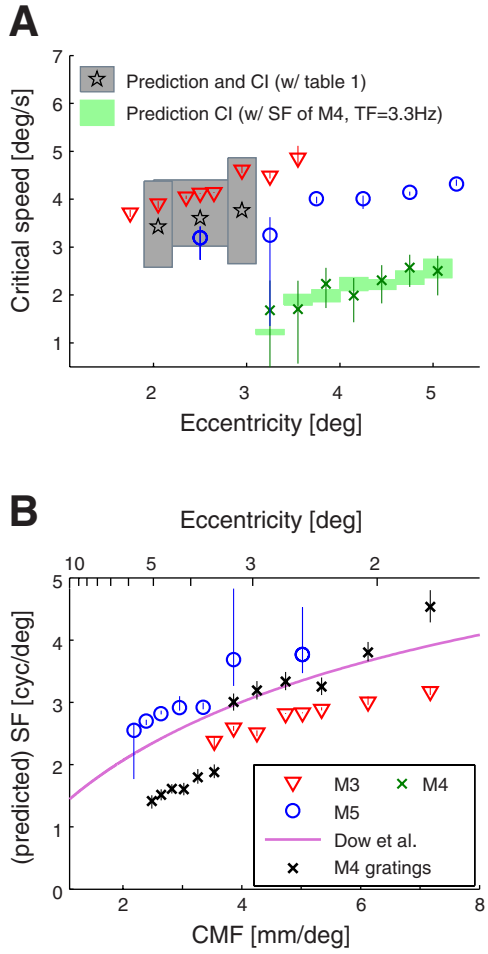


Fig. 4. Predicted and measured critical speed and prediction of spatial frequency preferences across monkeys. *A*: estimated critical speeds for 3 monkeys (*M3–M5*) across multiple eccentricities in V1 (see also legend in *B*). For each critical speed measurement, activation in pixels falling into 0.3° (*M3–M4*) to 0.5° (*M5*) eccentricity wide ROIs were pooled (critical speed measurements are plotted at the center eccentricity of their respective ROI). Exceptions are data points at 2.5° eccentricity which are calculated on 1° eccentricity wide ROIs (from 2°–3°). Confidence intervals (CI) are based on the 95% confidence bounds of the linear regression of t-values (see Fig. 3*B*). Predicted speed values are indicated with shaded areas and pentagrams. Gray shaded areas mark the CI of the model predictions using the receptive field (RF) parameters from Table 1. The prediction plotted at 2.5° is estimated on data from between 2° to 3° eccentricity. For the other two predictions (black pentagrams), the spatial frequency (SF) preference was reestimated on 0.3° wide regions (using responses to gratings in both monkeys *M2* and *M6*) while other RF parameters held constant (as in Table 1). Data from *M3* and *M5* correspond well with the prediction. Note that the predicted rate of change of the critical speed with eccentricity corresponds very well to the change of the observed critical speeds in all 3 monkeys. Light green shaded areas are CIs of model prediction based on SF preferences directly measured from *monkey M4* using grating stimuli (instead of *M2* and *M6* from Table 1; see black crosses in *B*). Temporal frequency (TF) preference was set to 3.3 Hz, which yielded a high correlation with the speed measurements in *M4* (other RF parameters taken from Table 1). In the predictions for *M4*, CIs were calculated without a CI for the TF preference since it was set to a fixed value (resulting in relatively narrower CIs). *B*: spatial frequency preference estimated with the spatiotemporal filter (STF) model and data from *A* (for monkeys *M3* and *M5*; *M4* omitted, because the temporal preference in this monkey did not correspond to the estimated model parameters, see DISCUSSION) vs. CMF. Red line: inverse RF size relation from (Dow et al. 1981).

For a drifting white noise luminance pattern, the critical speed $\mu_w$ can be approximately calculated as

$$\mu_w = c_w \frac{\omega}{\rho} \quad (2)$$

where $c_w \approx 1.5$ is a proportionality constant depending only on the bandwidth parameters (see APPENDIX for details). Thus in general, if a neural population is selective for larger spatial aspects (i.e., lower SF preference) or features shorter integration time constants (i.e., higher TF preferences) the critical speed is predicted to increase.

### *Estimation of the Parameter of the Model*

We chose to estimate the parameters of the STF model from our own experimental data. Note that without knowledge of the parameters the predicted speed cannot be obtained and model and experiment not compared. To achieve an independent estimate, we performed additional experiments using a different set of stimuli. We recorded responses to grating stimuli in two additional monkeys (*M2* and *M6*). In these experiments, optical recordings of V1 were made in response to moving full-field gratings of various SFs and TFs (25 combinations, see MATERIALS AND METHODS). Responses were trial averaged, and single condition orientation profiles were computed (see Fig. 7*A*, black curves). Because RF properties change with eccentricity (Dow et al. 1981; Foster et al. 1985; Van Essen et al. 1984), we pooled only cortical sites having eccentricity between 2 and 3° to achieve comparability between monkeys (the imaged regions overlapped across monkeys in this range). Since model responses to moving gratings can be derived mathematically (see APPENDIX), the theoretical equations of the grating responses were fit to the combined data of both macaques simultaneously (to yield suitable parameter across monkeys, see MATERIALS AND METHODS). Examples of the fitted response profile are displayed in Fig. 7*A* (red lines) together with the data (black lines). Note that orientation profiles are reasonably well fitted (86% correlation; see Table 1 for the resulting parameter values and individual error estimates). Figure 7*B* shows the goodness-of-fit landscape for two model parameters: preferred TF and preferred SF. The best fit of Fig. 7*A* is indicated (white circle) together with the error estimates (white bars). CIs were determined by searching those values along the axis of the parameter for which the error measure (one minus Pearson correlation coefficient) increased to 5% above its optimal value.

Estimated RF parameters are shown in Table 1. Spatial RF properties could be accurately estimated and the results are in accordance with spatial preferences reported for single units in the literature (see APPENDIX for a brief review). For instance, average preferred SFs of parafoveal recording sites in V1 were reported at 2.2 to 3 cycles/° (De Valois et al. 1982a; Foster et al. 1985), similar to our estimate of 3.28 cycles/°.

### *Comparison of Observation and Prediction*

To test how the STF model prediction compares to the experimentally measured profiles from drifting motion dots, we used the estimated RF parameters of Table 1 and calculated the expected response profiles for drifting random dots at the same speeds used in the experiments (see APPENDIX for a derivation of an analytic expression of the theoretical response

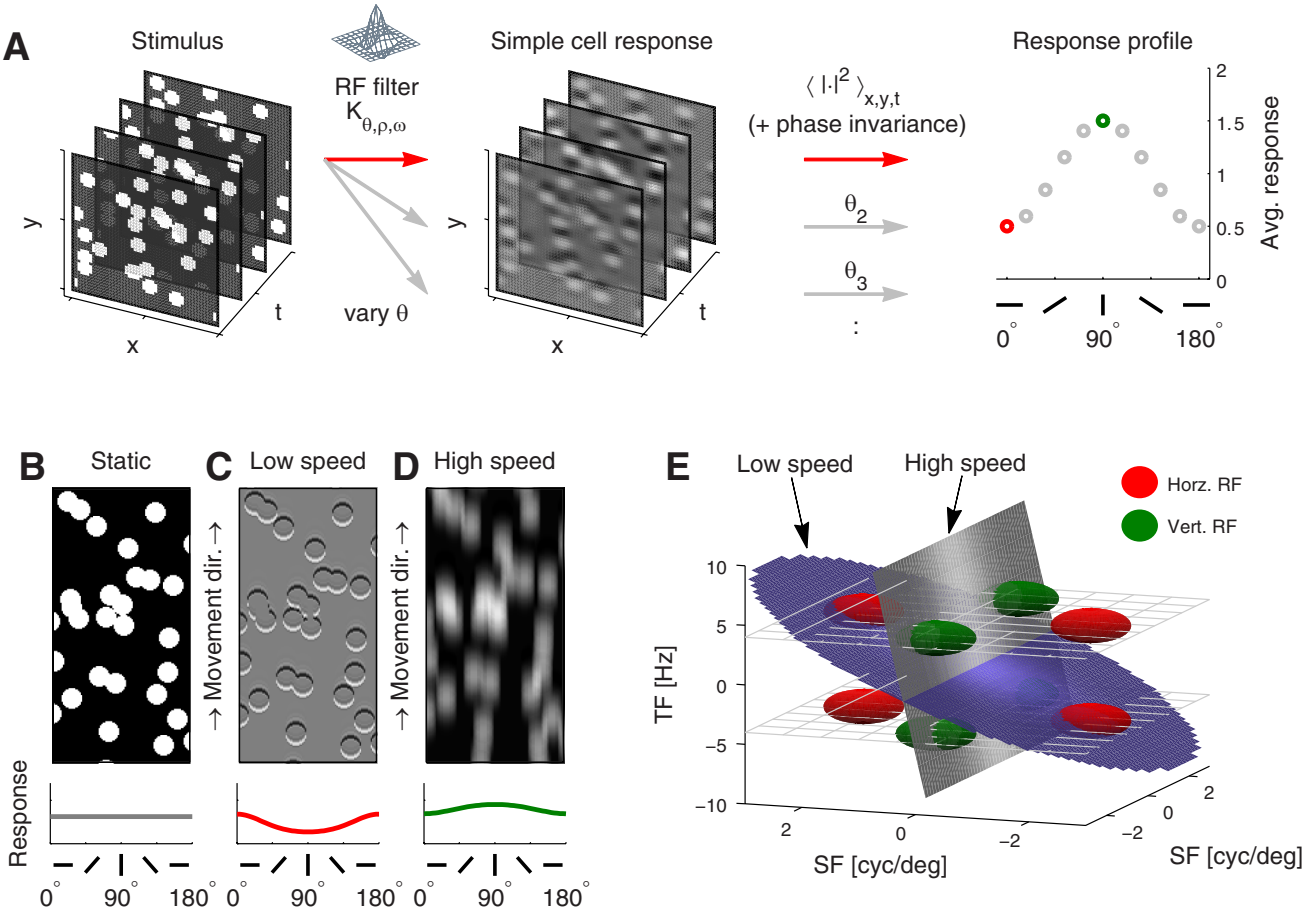


Fig. 5. Illustration of the STF model and qualitative explanation of responses to drifting dots. *A*: illustration of how to generate (single condition) orientation response profiles with the STF model. Stimulus is represented as a time varying luminance pattern. This input stream is filtered by spatiotemporal RF filters (Gabors). Filter output (at a given *x*, *y* value) corresponds to a particular simple cell response (at the same receptive field location) to the stimulus. To get the time- and population-averaged complex cell response, orthogonal oriented simple cells have to be squared and added and subsequently averaged over time and receptive field position. Repeating this process for different RF filter orientations results in an average orientation response profile for a given stimulus. *B–E*: qualitative explanation of the response profile inversion by the STF model. *B*: random dot stimulus, where dots move coherently upwards (dots enlarged). *C*: if motion is slow, the band-pass filter of a neural population acts as temporal high-pass filter. Therefore the border of the dots appears accentuated perpendicular to the movement direction inducing an orientation difference profile with peak at 0° (red curve). *D*: if motion is fast the band-pass filter of a neural population acts as temporal low-pass filter, integrating luminance along the path of movement. Elongated "motion streaks" now induce an inverted profile with peak response parallel to the axis of movements (90°; green curve). *E*: illustration in Fourier space. Power of a drifting stimulus is located on a tilted plane, the tilt angle depends on the movement speed. Gabor RFs are Gaussians in Fourier domain and indicated as blobs. While the "energy-plane" of the slow motion intersects only the red RF causing a strong response of the 0° domain, the fast motion intersects only the green RF, i.e., the 90° domain. The speed where both domains respond with equal strength is called the critical speed.

profiles to drifting dots). The predicted profiles for one monkey (*M3*) are plotted in Fig. 7, *C–E*. We found that the STF model predicted the average responses extraordinarily well (Pearson correlation 88%). Their visual appearance was very similar to the experimental recordings in Fig. 3*A*. Note that also the calculated profiles for individual speeds (Fig. 7*C*) matched the shape of experimental observations very well illustrating that responses were accurately predicted across orientation domains.

The relative response amplitudes for different speeds were well predicted [Fig. 7*D*; Pearson correlation 77% (CI: 60. . .87)] . For speeds >4°/s, amplitudes increased gradually reaching maximal values at around 16°/s. For speeds below the critical speed of ~4°/s, there seemed to be a slight underestimation of the amplitudes. This could be caused by a small deviation of physiological RFs from Gabor shapes used in our model (see DISCUSSION). Similarly, if one computes the circular mean angle $\alpha$ of the difference profiles [restricted to the interval from 0 to 90°, i.e., $(a - 90°)/2$] to access the angular position of the peak response along the orientation axis, we found that the peak position as function of velocity were well captured by the model [Fig. 7*E*; Pearson correlation 87% (CI: 76. . .93)]. In particular, peak positions changed rapidly around the critical speed at ~4 °/s from 0 to 90° in both model and experiment indicating the abrupt inversion of the difference profile.

Having established that predicted response profiles were similar in theory and experiment, our next goal was to establish a CI of critical speeds based on the STF model and compare the predictions across monkeys. Measurements of the critical speed should fall in this CI if the STF model would be appropriate. We calculated that, in the eccentricity range of 2 to 3° (where the model parameters were fitted to), the predicted critical speed was 3.6°/s (CI: 3.0···4.4°/s; CI was estimated by conservatively computing the critical speed when each parameter was changed to either of its own confidence bound individually and taking the "worst case" smallest and highest values). We found that with the

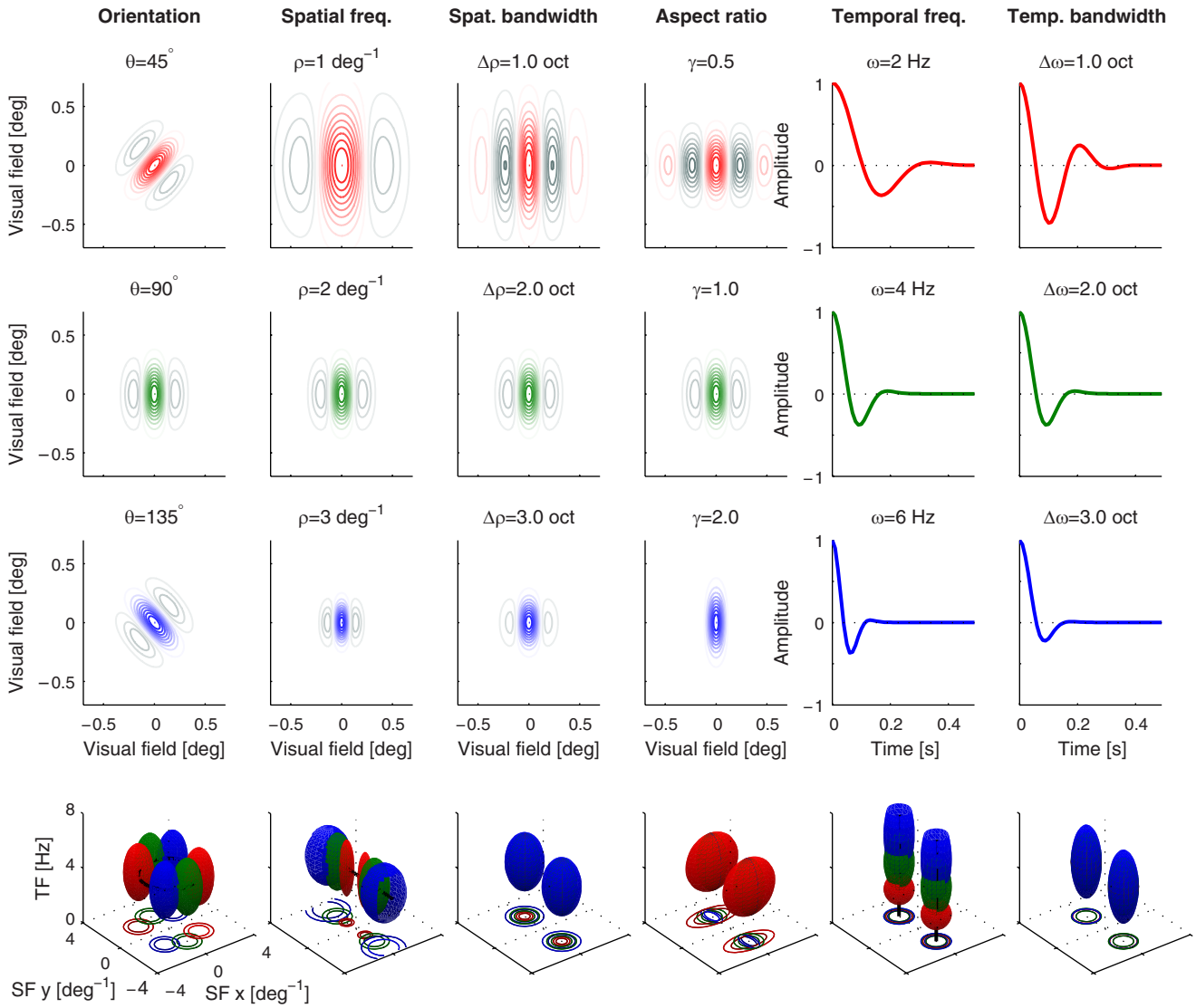


Fig. 6. Varying the 6 receptive field parameters of the STF model. Neural receptive fields are defined by (spatiotemporal) Gabor functions. Note that the temporal RF is represented by a Gabor function as well and is only plotted for positive times. In each column, a single parameter is varied (as indicated at *top*) and the appearance of the respective receptive fields are illustrated (colored contour lines represent positive activation). Last row of plots illustrate the receptive fields in Fourier domain. Gabor RFs are Gaussians in Fourier domain, the ellipsoid of its standard deviation is displayed. Colors indicate orientation domains. Note that our RFs are nonselective for directions causing a second, mirrored RF region in Fourier space. Negative TFs are omitted here for illustration purposes.

exception of one monkey (*M4*; see DISCUSSION), the measured critical speeds in V1 indeed fell within the confidence region of the prediction when the eccentricity range of the measurements was matched to that of the model parameter estimates (predicted critical speed is marked with a black pentagram at 2.5° and the confidence region is indicated as a gray area in Fig. 4*A*). Note that although *monkey M1* (from Fig. 1) showed a similar critical speed of slightly >4°/s, this value is not directly comparable to that reported in Fig. 4*A* because profiles were pooled over a larger eccentricity region (in this experiment only approximately known to come from within a range of ~2–6°) and dot sizes were somewhat larger than in *monkeys M3–M5*.

To test whether the observed changes in critical speed with eccentricity in V1 are in accordance with the STF model, we refitted the SF preferences in two ROIs in *monkeys M2* and *M6* when only taking a narrow range of eccentricities at the borders of our initial ROI into account (1.9–2.2° and 2.8–3.1° eccentricity, respectively), while leaving other RF parameters constant (as in Table 1). We found that the predicted critical speed based on these new model parameters changed with eccentricity, in accordance with the measurements (see Fig. 4*A*, black pentagrams). The predicted rate of change was 0.4 Hz ([°/s/°] = [Hz]) (CI: 0.25···0.51 Hz, CI: based on 95% CI of the linear regression), which was in good agreement with rates of change observed in all monkeys [in Hz: *M3*: 0.6 (0.51···0.73), *M4*: 0.5 (0.25···0.76), *M5*: 0.4 (0.27···0.59)].

To further analyze changes with eccentricity, we computed a prediction of the SF preference from the critical speed measurements using the STF model. Specifically, we used the equation for the theoretical responses and searched for the SF preference, which would predict the observed critical speed measurements when other parameters were held fixed (as in Table 1). In Fig. 4*B*, resulting values are plotted vs. the cortical magnification factor, which can be related to eccentricity (Tootell et al. 1988). Although somewhat scattered (most likely due to the interanimal variability), the predicted SF was in the

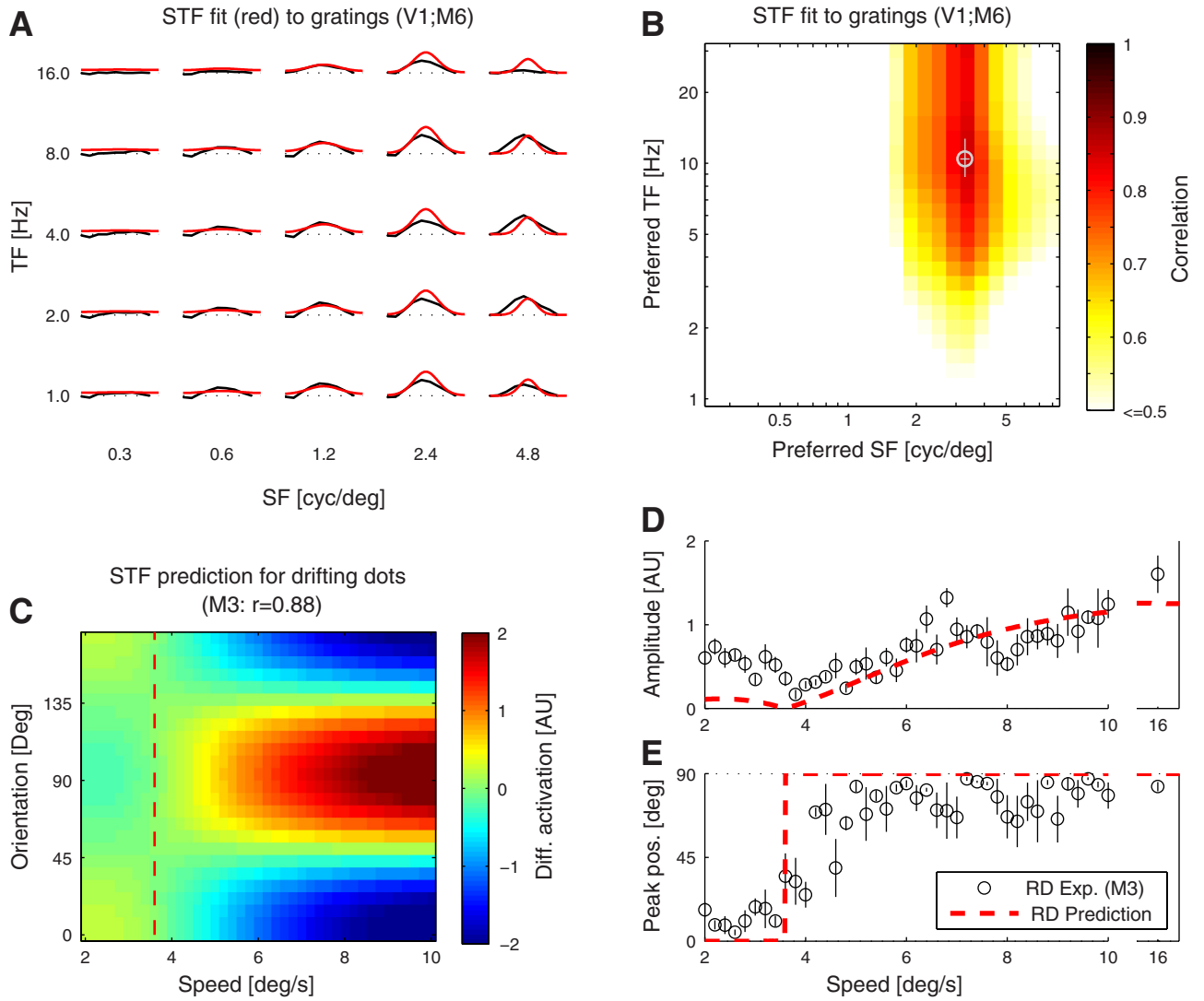


Fig. 7. Estimation of model parameters and theoretical prediction of the average response profiles to drifting random dots. *A*: single condition orientation profiles in V1 to gratings of various spatiotemporal frequencies. STF model (red lines) was used to simultaneously fit the grating responses in *monkeys M2* (black lines) and *M6* (not shown). For estimated model parameters refer to Table 1. *B*: goodness-of-fit landscape for data in *A*. White circle and lines: best fit and CI, respectively. *C*: predicted profiles to drifting random dots, when using the estimated RF parameters (88% correlation with data from *monkey M3*; compare to Fig. 3*A*). *D* and *E*: comparison of amplitude and angular position of the peak difference response of the prediction to the data from *monkey M3*. Prediction (dashed lines) captures the observation very well. Note that we do not simply fit the model to the data here but instead predict responses, since model parameters were estimated from independent measurements (for details see RESULTS).

correct range for two monkeys (*M3* and *M5*) and clearly increased with cortical magnification factor in a similar form as published values of RF sizes (Dow et al. 1981; magenta line) and direct measurements of the population SF preference using full-field gratings (black crosses) suggest.

### *Inferring RF Properties Using the STF Model and Drifting Dots*

Our results indicate that the STF model is able to accurately describe the average population response recorded with intrinsic optical imaging in V1 of macaques. Because of this good quantitative agreement, we can use the STF model as a tool to infer new information about the RF properties of the recorded neural populations. In principle, fitting the model to the experimental observations will yield estimates of all of the six model parameters (see Fig. 6). In the following, we show that fitting responses to random dot motion is particularly useful for estimating the TF preference with high accuracy in case if the SF preference is already known (for instance from a SF gratings experiment).

Since the critical speed mainly depends on the ratio between spatial and TF preference (see *Eq. 2*), this ratio is well accessible using the motion streak paradigm. To infer RF parameters from the motion response data, we therefore fitted responses to drifting random dots stimuli with our derived theoretical response equation and performed a search in the parameter space of the model to find the best match between theory and experimental orientation profiles. Since the bandwidth parameters seemed to be rather constant across monkeys, we fixed these parameters to literature values $\Delta\rho = 1.7$ and $\Delta\omega = 3$ octaves, and $\gamma = 1$ (De Valois et al. 1982b; Foster et al. 1985). With the bandwidth parameters fixed, only the SF and TF preferences were left to vary. The SF and TF preference values of the best match then can be regarded as an estimate of the RF

Table 1. *Model parameters*

| Parameter | Symbol, Unit | Fitted Values (CI) |
|---|---|---|
| Goodness of fit (correlation) | $r$ | 86% |
| Spatial frequency preference | $\rho$, cycle/° | 3.28 (3.13, 3.44) |
| Temporal frequency preference | $\omega$, Hz | 10.4 (8.8, 12.7) |
| Spatial frequency bandwidth | $\Delta\rho$, octaves | 1.57 (1.38, 1.77) |
| Temporal frequency bandwidth | $\Delta\omega$, octaves | 6.5 (3.8, 10*) |
| Aspect ratio | $\gamma$ | 1* (1*, 1.14) |
| Predicted critical speed | $\mu$, °/s | 3.7 (3.0, 4.5) |

Model parameters estimated from responses to spatiotemporal grating stimuli (see Fig. 7, *A* and *B*) in two monkeys (*M2* and *M6*). Because both monkeys had slightly different chamber positions, care was taken to only include data from overlapping cortical positions with eccentricity between 2 and 3° in V1. Fits were obtained by using data from both monkeys simultaneously to ensure that estimated parameters are constraint across monkeys. During fitting, parameter ranges were constrained by physiological limits (see materials and methods). Values on these limits are marked with asterisks. Confidence intervals (CI) were determined by searching those values along the axis of the parameter for which the error measure (1 − Pearson correlation coefficient) increased by 5% above its optimal value. Predicted critical speeds are based on the estimated model parameters. Confidence intervals for the critical speeds were estimated by computing the speeds when each estimated parameter is changed to either of its confidence bounds individually and by then taking the "worst case" smallest and highest values.

properties of the recorded neural population. The resulting best match to data from *monkey M1* (Fig. 1) is plotted in Fig. 8*A*. The predicted response profiles matched the experimental data very well (95% correlation), despite the fact that the fit had only two degrees of freedom. This good fit further corroborated the quantitative usefulness of the STF model.

The goodness-of-fit landscape in two parameters, TF and SF preferences, is shown in Fig. 8*B*. Parameters used for the fit in Fig. 8*A* are indicated with a blue square. Confidence regions of literature values and estimates from Table 1 are indicated with gray and green ellipses, respectively, and overlap well with high goodness-of-fit values, indicating that a fit to motion data yields realistic estimates. Note that in the log-log plot of the goodness-of-fit landscape, parameter combinations that approximately lie within a linear tube of slope 1 were all equally suitable to fit the data, because these values have a constant ratio of TF to SF preference (compare to *Eq. 2*). For high SFs and TFs (or for larger dot sizes), the white noise approximation (*Eq. 2*, dashed-dotted line) is not suitable because it is only valid in the limit of small dots (see derivation in the APPENDIX). The more accurate approximation in the case of random dots (*Eq. 1*) is able to track the deviation (solid line).

From the resulting fit, one can estimate the ratio of the TF to SF preference of the underlying neural population with great accuracy. We found 3.67°/s (3.52···3.82°/s; CI was estimated on a line orthogonal to the line of constant speed ratio). Note that the relative error is <5%. This accuracy would be difficult to obtain when using only data derived from gratings stimuli instead of fitting the dot motion data. If one directly computes the ratio from gratings experiments by dividing the estimates for the preferred SF and TF one finds a ratio of 3.2°/s with a much larger relative error deviation of 24% [added relative errors of the SF (0.05) and TF (0.19) preferences from Table 1]. This larger relative error is mainly due to the difficulties in estimating the TF preference from grating responses because of the large temporal bandwidth of typical V1 neurons.

In contrast to the TF preference, the SF preference can be accurately estimated using the traditional gratings paradigm, since the SF bandwidth is relatively narrow (having a relative error of 5%, see Table 1). Thus one can use the SF preference from a gratings experiment together with the fit to motion response data to yield a more accurate estimate of the TF preference than obtainable from a traditional gratings design alone. For instance, if we take the SF preference and the CI interval from Table 1 as reference, we find from the fit to the motion responses (Fig. 8*A*) that the TF preference in *monkey*

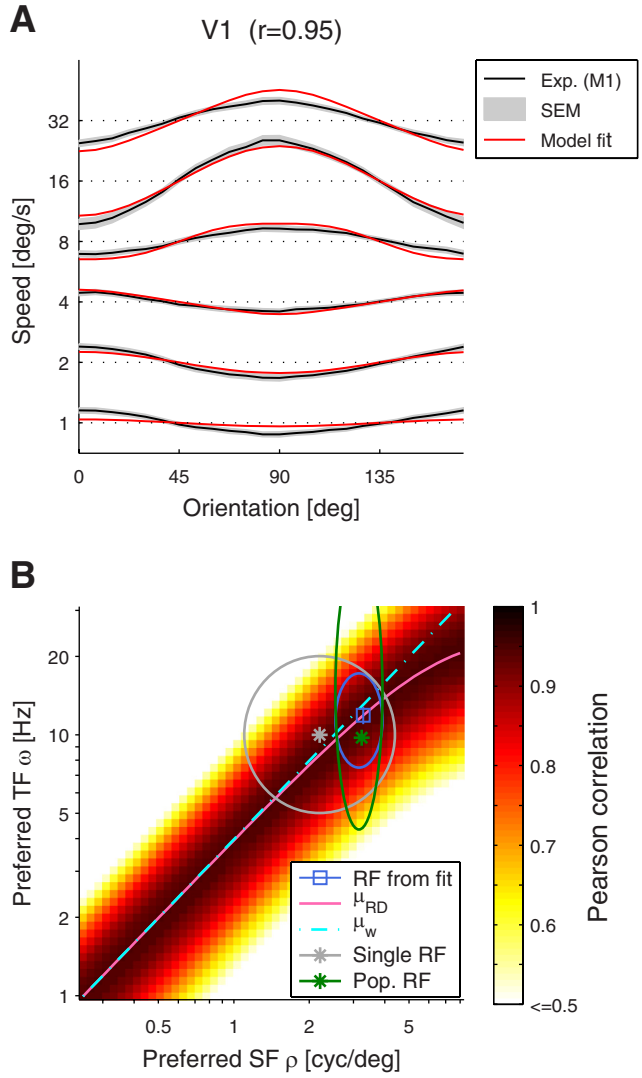


Fig. 8. Estimating spatiotemporal RF parameters by using the drifting random dot stimuli ("motion streak" paradigm) and the STF model equations. *A*: mean response profiles measured in *monkey M1* (black lines; same data as in Fig. 1) fitted by the STF model for 6 speeds of motion (red curves). The (Pearson) correlation between model fit and data is 95%. *C* and *D*: goodness-of-fit landscapes. Blue square dot: parameters used in *A* (i.e., the best fitting TF preference; SF preference as in Table 1). Blue ellipse shows the CIs of the TF preference estimation using the "motion-streak" paradigm. RF parameter estimates and CIs from the grating experiment (from Table 1) are plotted in green ("Pop. RF"). Both confidence ranges are here calculated as the region where the goodness-of-fit value (Pearson correlation) remains >90% of that of the best match. Literature RF parameter from electrophysiological recordings in single neurons are plotted in gray ["Single RF"; SF from Foster et al. (1985) and TF from Hawken et al. (1996) and Levitt et al. (1994)]. Elliptic regions indicate literature reported standard deviations. Additionally, the theoretical approximations for random dots (*Eq. 1*; solid line) and white noise (*Eq. 2*; dashed-dotted line) are shown for parameter values having the same critical speed as the best match (blue square).

*M1* should be 11.9 Hz (11.0···12.8 Hz, CI calculated as in Table 1). If one uses a more conservative criteria to define the CI (as in Fig. 8*B*: the range where the Pearson correlation is >90% of its optimal value), the CI increases only to 7.5···17 Hz. On the other hand, in the case of the TF preference estimation from the gratings experiment (Table 1), the CI increases to 4···50 Hz using the same criteria (compare the blue and green error ellipses in Fig. 8*B*). Thus our motion streak paradigm constrains the TF preference estimation more than fourfold compared with the traditional grating setting.

Taken together, given that the STF model accurately describes the data, we can use the motion streak paradigm to estimate temporal RF properties of the underlying neural population more accurately than possible with traditional gratings stimuli alone.

## DISCUSSION

We previously reported the presence of axis-of-motion maps in V1 of the macaque (Lu et al. 2010). In this study, using optical imaging, we demonstrate velocity as well as eccentricity dependency of axis-of-motion maps in V1 of the macaque monkey. These observations are consistent with the motion streak response (Burr and Ross 2002; Geisler 1999; Geisler et al. 2001). We show that orientation response profiles and the critical speeds can be accurately measured with optical imaging techniques across varying eccentricities in V1. Importantly, the critical speed is not only sensitive to slight changes of RF properties of the neural population but can also be calculated using the STF model. Thus a critical speed measurement opened two opportunities. First, it established a quantitative test of the adequateness of the STF model for average population responses. Second, the measurement of the critical speed (and the orientation response profiles) can be used to infer RF properties of the underlying neural populations using motion stimuli. We found that our approach is sensitive enough to detect the change of population RFs with eccentricity as expected from single unit recordings. In monkeys, imaged regions commonly span several degrees eccentricity; however, to our knowledge a change of RF properties was not previously investigated using optical imaging where data are often pooled to increase the signal-to-noise ratio but possibly confining interpretations.

### *Quantitative Agreement of the STF Model*

We found that the STF model was in good quantitative agreement with the optical imaging data in V1 of macaques. The model not only predicted the correct range of critical speeds for most animals, it also very well explained the observed shape of the differential response profiles. A direct comparison of the agreement of population data in macaques had been missing, since almost all previous studies analyzing population activity with the STF model have been either purely experimental studies or purely modeling studies. However, one study (Zhang et al. 2007) tested the correspondence of the SF responses of the STF model with optical imaging data in cats and found a good agreement corroborating our findings in macaques. Their approach was different in that they did not measure the reversal point of the response (the critical speed) to drifting dot motions but analyzed responses to sinusoidal and square-wave patterns instead. The advantage of drifting dots is that it leads to an inversion of the response at a precise speed, which can be determined with high accuracy even in noisy data (as established here). Because the critical speed can be measured very exactly in both experiment and model, our criteria was more demanding and represents a new approach. The sensitivity of our approach is clearly evident in the need to carefully restrict the eccentricity range for which we compared model and experiment. Moreover, in contrast to Zhang et al., we extended the comparison to additionally account for the orientation responses and changes in RF properties with eccentricity. Together, results of both studies suggest that the STF population response model is valid across multiple species and domain types and provides a general description of how dot motion is represented in visual cortex.

We demonstrate for the first time that the critical speed depends on eccentricity in V1. This dependency likely arises from the known decrease of the preferred SF of single neurons with growing eccentricity (Dow et al. 1981; Foster et al. 1985; Van Essen et al. 1984) and was very well predicted by the STF model. In fact, if one uses *Eq. 1* to relate measured critical speeds with SF preferences across eccentricities (using data of *monkey M4* in Fig. 4, *A* and *B*), the dependency on eccentricity vanished (testing for linear trend, $P = 0.58$).

Although we used similarly small dot sizes across all experiments presented in this study, one can nevertheless predict the effect of changing the size of the dots in the random dot motion stimuli from *Eq. 1*. It turns out that a change in dot size (represented by $\alpha$ in *Eq. 1*) is predicted to affect the critical speed. With the use of the RF parameters of Table 1, increasing the dot radius from, e.g., 0.05 to 0.5°, should increase the critical speed roughly linearly with a slope of ~25°/s per dot radius degree. Thus using for instance a dot radius of 0.2° in respect to 0.1° should increase the observed critical speed by ~2.5°/s. Therefore, changing the SF composition of the stimulus will have profound influence on the measured critical speed.

On the other hand, changing the density or contrast of the stimulus pattern should, in first approximation, not affect the critical speed. Dot density or response magnitudes are not represented in *Eq. 1* because only difference responses are considered. Taking the difference of two perpendicular movement responses effectively cancels response magnitudes out of the equation.

In addition to V1, we also found that V2 exhibits robust axis-of-motion maps and that map inversion occurs for increasing motion velocities (data not shown). It is conceivable that some parts of V2 show a similar response profile inversions due to the direct input of V1. To analyze and interpret V2 responses in detail, however, an extension of the STF model to include higher visual areas would be desirable and necessary.

### *Variations Among Animals*

Our measurements reveal critical speeds of ~4°/s for different sites in V1. This speed was consistent across three monkeys (*M1*, *M3*, and *M5*) and fell into the CI of STF model prediction. We took the approach to estimate the model parameters from additional grating experiments. This approach has the advantage to offer independent estimates of the parameters and thus renders the calculated critical speed a true prediction and not a simple fit to the data. Moreover, we

estimated the parameters from two further monkeys (*M2* and *M6*) to achieve a generalization over different animals. Relying on data from different animals might be similar to the situation where one wants to apply the STF model as a "null hypothesis" model to contrast and interpret responses to complex stimuli. Because of experimental time restrictions, extensive RF measurements (i.e., measuring both TF and SF preferences) might only be attempted in one animal or RF values might be preferably taken from the literature. While the latter was too restrictive here because literature values are usually pooled across many eccentricities, we found that the former approach yielded surprisingly good agreement across monkeys. We here provide these RF estimates for a narrow eccentricity range (2–3°) pooled over two monkeys (Table 1). These values could be used when applying the STF model to other data. In one monkey (*M4*), however, we found a significantly lower critical speed (~2°/s). The SF preference in this monkey did not differ from the *monkeys M2* and *M6* when measured with gratings (around 3 cycles/° at 2–3° eccentricity; see Fig. 4*B*). Therefore, it is likely that other RF parameters in this monkey were significantly different from that of the other monkeys in this study. Since the critical speed is very sensitive to changes in TF preference, a systematic variation in *M4* would result in a discrepancy of the observed critical speed. In fact, a TF preference of ~3.3 Hz in *M4* (as opposed to values ~10 Hz in other monkeys) would very well explain the low critical speed measurements (see Fig. 4*A*, confidence values of the critical speed predictions using the alternative TF preference as model parameter are displayed as green bars). Note that even in the literature on single neurons, both a TF preference of 3.7 Hz (Foster et al. 1985) and values ~10 Hz (Hawken et al. 1996) are supported for V1 in macaques, suggesting that TF preference might indeed be a parameter with a bimodal variability between individual animals.

### *Model Considerations*

We derive new analytic equations describing the population response to drifting dots. Previous studies (Mante and Carandini 2005, Baker and Issa 2005) were limited to numerical calculations. These analytic equations lead to a qualitatively improved model fitting that enables the inference of RF properties from the optical imaging data. This inference of RF properties from complex optical imaging responses demonstrated in our study is a new concept. It has not been investigated or discussed by the previous studies.

We also examined whether the fit could be improved with adjustments to the shape of the RF filter. We here used classical Gabor functions as spatial RFs (Jones and Palmer 1987). However, there are some disadvantages to using Gabor-shaped filters for explaining experimental data or coding natural scene information (Field 1987; Hawken and Parker 1987; Stork and Wilson 1990). In particular, unlike experimental data, low frequency components are passed too readily by Gabors as they include a strong DC component (mean). To overcome these disadvantages, other RF filters have been proposed, such as Log-Gabor or Difference-of-Gaussians (Field 1987; Hawken and Parker 1987). We tested whether modified RF structures would improve the fit to the data (on single condition optical imaging responses in V1 to gratings of 6 different SFs) and found that correlations could be improved from 82% (Gabor RF) to 96% for alternative RF structures (see Fig. 9). However, when fitting the drifting dots data from Fig. 8 with these alternative RF structures, the overall fit was not significantly improved. This suggests that, in cases where the nonorientated DC component is largely subtracted out by taking the difference between two orthogonal conditions, Gabor RFs are already a very good model. Moreover, because Gabor RF additionally allow the response equations to be solved analytically, we chose to use Gabor RF filters in our derivation of the STF model.

For mathematical convenience, we modeled the temporal response as a Gabor function as well, as was done previously (Adelson and Bergen 1985; Grzywacz and Yuille 1990). However, it is known that physiologically the temporal response is better fitted by other functional forms (Adelson and Bergen 1985; Robson 1966; Watson and Ahumada 1985). In particular, Gabor functions are nonzero for negative times and therefore noncausal filters. However, since on average the TF information does not change in our stimulus paradigm (the dots are drifting with constant speed), causality is of no concern here. We also did not need to include nonlinear contrast gain control [such as divisive normalization (Heeger 1992)] because we investigated stimuli of identical and fixed contrast.

### *Inferring Population RF Properties Using Complex Stimuli*

Given our results that the STF model provides a good quantitative description of optical imaging responses in V1, one can use the motion stimulus paradigm for the estimation of temporal RF parameters otherwise not easily accessible with intrinsic BOLD methods. If one had information of the SF preferences available (for instance by fitting gratings responses of different SFs as can be accurately done), we showed that measuring the critical speed would be an alternative way to accurately estimate the TF preference in V1. Note that the critical speed according to *Eq. 2* is approximately proportional to the TF preference with proportionality constant of ~1 (for typical RF values in V1). Thus a change in TF preference will results in a change of the critical speed of the same order of magnitude. In contrast, when we estimated the TF preference using the traditional grating paradigm, doubling the TF of the gratings almost did not change the response profiles due to the wide temporal band-pass property of V1 neurons (see, e.g., Fig. 7*A*), rendering the estimation of the TF preference very difficult when relying on gratings. We found that this large uncertainty in TF preference estimation can be reduced drastically if relying on motion responses.

We here showed that inference of RF parameters during more complex stimuli presentation might outperform traditional grating settings. Additionally, one could extend our method to use drifting patterns of, for instance, naturalistic noise (Field 1987) or natural images, with the additional advantage that the RF properties are estimated within a realistic stimulus regime instead of being based on rather artificial responses elicited by gratings. In fact, the accuracy of measuring temporal aspects of RF properties with this approach is remarkable because the temporal resolution of the optical imaging method is intrinsically slow (a few to several seconds). The crucial feature for yielding high accuracy is that spatiotemporal interactions are projected onto the orientation axis; in this way, the spatial resolution of the optical imaging

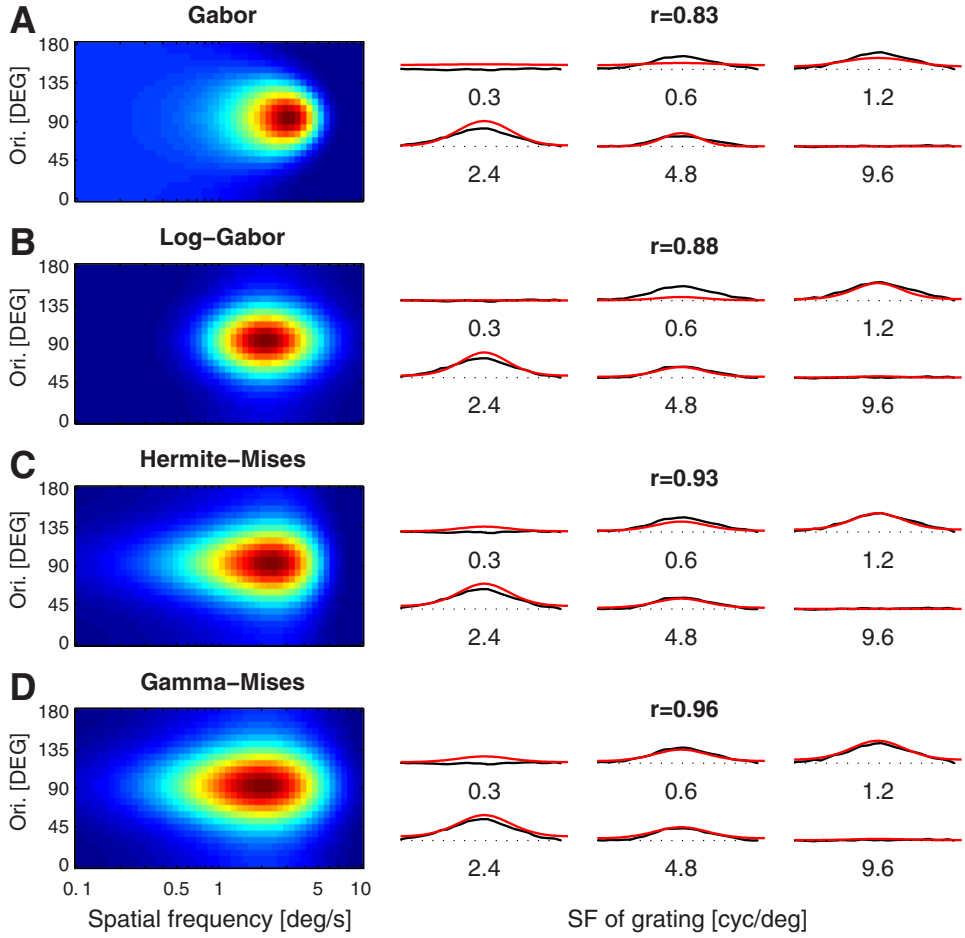


Fig. 9. Alternative RF structures result in superior fits to single condition maps at the population level. Here, we tested 3 possible modifications of the spatial RF. All 3 modify the form of the standard RF (*A*) along the radial spatial frequency axis in frequency domain. In all 3 modifications, the orientation component was chosen to be of the shape of a Mises distribution, which resembles a rotational Gaussian function. *A*: Gabor RF. Note the nonorientated DC-component. *B*: log-Gabor RF resembling a Gaussian function for logarithmic radial SF as suggested by (Field 1987). *C*: hermite function of order one suggested by (Stork and Wilson 1990). *D*: new RF form defined by the shape of the Gamma-distribution on the radial SF axis. All the above functions had only 2 free parameters, the mean and the bandwidth. Variance was chosen to ensure a constant bandwidth over a range of preferred frequencies. *Left*: predicted responses of the RFs, which yielded the best match to single condition responses to gratings of 6 different spatial frequencies. *Right*: experimental responses to gratings (black curves) and model fit to the data (red curves). Gamma-Mises RFs perform best, improving the fit to the single condition responses significantly compared with the Gabor RF in *A*.

method can be exploited to measure temporal response properties of the underlying neural populations.

## APPENDIX

### *Average Neural Response*

In the classical filter model of the visual system (Hubel and Wiesel 1962; Movshon et al. 1978; Adelson and Bergen 1985; Watson and Ahumada 1985; Mante and Carandini 2005), the responses of simple neurons are proportional to the local luminance intensity falling in the RFs of the neurons and is calculated as the convolution of the RF filter kernel $K = K(x, y, t; x', y', t')$ and the stimulus $S = S(x', y', t')$, namely $r_s(x, y, t) = S * K$. The average response of neurons having different preferred positions in visual space, but otherwise the same RF properties, is proportional to the integral of the responses over visual space and time. Neglecting constant factors for simplicity, we thus can write the average activity as $\langle r_s \rangle = \int S * K \, dx \, dy \, dt$. However, because the optical imaging method mostly records activity of the exposed upper layers of the cortex, the measured responses will mostly reflect the activity of complex cells (Martinez et al. 2005). Complex neuron responses are commonly assumed to be proportional to the luminance energy, which is related to the square of the output of simple cells. This is called the energy mechanism (Adelson and Bergen 1985).

The average response of complex cells is therefore related to the integral of the square of the response of simple cells. However, we do not have yet respected the phase invariant property of complex cells, which is assumed to arise by summing input from phase-shifted simple cells, also called quadrature pair (Adelson and Bergen 1985). Changing to the Fourier domain, it is straightforward to include the phase invariance responses of complex cells by setting

$$\langle r_c \rangle^2 = \int \left| \mathcal{F}\{S\} \right|^2 \left| \mathcal{F}\{K\} \right|^2 d\xi_x d\xi_y d\xi_t \qquad (A1)$$

The product of the absolute values ensures that the phase of the RFs optimally match the phase of the stimulus thereby maximizing the response (Cauchy-Schwartz Inequality). We use *Eq. A1* to model the average response of complex cell populations (Adelson and Bergen 1985; Mante and Carandini 2005). Intuitively, the average neural response is calculated by averaging the energy of the stimulus, which falls in the RF of the neural population in the Fourier domain.

### *Receptive Fields*

We next consider how to choose the RF filter $K$ according to physiology. It is well known that the shape of classic RFs in V1 resemble Gabor functions (Jones and Palmer 1987). A Gabor function is a sinusoidal wave multiplied by a (normalized) Gaussian. In complex terms, it can be expressed as (Movellan 2002):

$$G(\mathbf{x}) = \left| 2\pi\Sigma \right|^{-\frac{1}{2}} \exp\left( -\frac{1}{2}\mathbf{x}^T\Sigma^{-1}\mathbf{x} + 2\pi i \boldsymbol{\rho}^T\mathbf{x} \right) \qquad (A2)$$

The frequency vector $\boldsymbol{\rho} = (\rho_x, \rho_y)^T$ simultaneously defines the preferred (radial) frequency, $|\boldsymbol{\rho}|$, and the preferred orientation $\theta = \tan^{-1}\frac{\rho_y}{\rho_x}$ of the neural population. The Gaussian envelope of the sinusoidal is defined by the covariance matrix $\sum$. It is known from experimental observations (Ringach et al. 2002) that the envelope might be slightly elliptic, where the shorter half-axis of the ellipse *a*

is in the direction of the frequency normal $\boldsymbol{\rho}$. Thus it is convenient to switch to polar coordinates, $\rho$ and $\theta$, write $\boldsymbol{\rho} = \rho\,(\cos\,\theta,\,\sin\,\theta)^T$ and rotate the covariance matrix according to the RF orientation, $\sum = R(\theta)^T\,\mathrm{diag}\,[(a^2, b^2)]\,R(\theta)$ where $R(\theta)$ is the two-dimensional rotation matrix. The half-axes $a$ and $b$, with $b \geq a$, define the shape of the Gaussian envelope. To use physiological meaningful parameters, one can show (Movellan 2002) that, with the definition of an aspect ratio $\gamma \equiv b/a$, $a$ and $\gamma$ are related to the half-magnitude frequency bandwidth $\Delta\rho$ (in octaves) and the half-magnitude orientation bandwidth $\Delta\theta$ in the following manner. With constant $k_\rho \equiv (2^{\Delta\rho} - 1)/(2^{\Delta\rho} + 1)$, it is

$$\mathrm{a} = \frac{\sqrt{\log 4}}{2\pi\rho\mathrm{k}_\rho} \tag{A3}$$

And

$$\gamma = \frac{\mathrm{k}_\rho}{\tan\left(\frac{1}{2}\Delta\theta\right)} \tag{A4}$$

Thus one can use physiological meaningful parameters to set up the model (see below).

The temporal response profile of a neuron in V1 typically consists of an excitatory drive followed by a weak inhibition. This phasic response property can be idealized as a temporal Gabor function $G(t)$ (Adelson and Bergen 1985), with standard deviation $\sigma_t$ and TF $\omega$. Analogous to the SFs (*Eq. A3*), one can relate the standard deviation $\sigma_t$ to the half-magnitude TF bandwidth $\Delta\omega$ (expressed in octaves). With the constant $k_\omega \equiv (2^{\Delta\omega} - 1)/(2^{\Delta\omega} + 1)$

$$\sigma_\mathrm{t} = \frac{\sqrt{\log 4}}{2\pi\omega\mathrm{k}_\omega} \tag{A5}$$

If we for simplicity assume separable temporal and spatial filters, the overall spatiotemporal RF can thus be expressed as a three-dimensional Gabor function $K(x, y, t) = G(x, y)G(t)$.

Conveniently, the Fourier transform of a Gabor function results in a Gaussian function in frequency domain. Its standard deviations are proportional to the inverse of the standard deviations in the spatial domain, and its mean is centered at the preferred spatial and TF of the RF. For the two-dimensional spatial RF with $\boldsymbol{\xi} = (\xi_x, \xi_y)^T$, this yields

$$\left|\mathcal{F}\{\mathrm{G}(\mathbf{x})\}(\boldsymbol{\xi})\right| = \exp\left[-2\pi^2(\boldsymbol{\xi}-\boldsymbol{\rho})^\mathrm{T}\Sigma(\boldsymbol{\xi}-\boldsymbol{\rho})\right]. \tag{A6}$$

The Fourier transform for the temporal filter is computed analogously. With these derivations we can write for the average neural response

$$\langle \mathrm{r_c}\rangle^2 = \int \left|\mathcal{F}\{\mathrm{S}\}\right|^2 \exp\left[-4\pi^2(\boldsymbol{\xi}-\boldsymbol{\rho})^\mathrm{T}\Sigma(\boldsymbol{\xi}-\boldsymbol{\rho}) - 4\pi^2\sigma_\mathrm{t}^2(\xi_\mathrm{t}-\omega)^2\right]\mathrm{d}\xi_x,\,\mathrm{d}\xi_y,\,\mathrm{d}\xi_\mathrm{t} \tag{A7}$$

Taken together, the RF is defined by its preferred orientation $\theta$, (radial) SF $\rho$, and TF $\omega$, and the respective half-magnitude bandwidths $\Delta\theta$, $\Delta\rho$, and $\Delta\omega$.

For simplicity of the equations, our derivation of the response $\langle \mathrm{r_c}\rangle = \langle \mathrm{r_c}(\theta, \rho, \omega)\rangle$ in *Eq. A7* started from a complex Gabor function *Eq. A2* and thus does not show invariance of the response to a rotation by 180° in visual space or to a 180° switch in the movement direction. If the Gabor function is composed of a real sine function (as in physiology), then the Fourier transform *Eq. A6* is given by the average of two Gaussians, one centered at $\rho$ the other mirrored at $-\rho$. Multiplication with the two similarly mirrored temporal RF results in altogether four Gaussian blobs in frequency space. Calculating the power (*Eq. A1*) further introduces additional cross multiplication terms between any two blobs if the Gaussian blobs overlap significantly in frequency space [see Jones and Palmer (1987) and Grzywacz and Yuille (1990) for a derivation starting from real-valued Gabors]. We use the full equation for the response in RESULTS, but neglect the residual cross-terms for the derivation of the critical speed expression (see below). This approximation is valid if the Gaussian blobs are far apart and nonoverlapping (for instance if having a small bandwidth) in which case the values of the residual cross-terms get negligibly small.

### *RF Parameters in the Literature*

Since we defined the RF in a physiologically meaningful way, literature parameters could be used to define reference RFs for V1 and initialize the STF model. However, since parameter values have been estimated on single units electrophysiological recordings rather than optically imaged responses of neural populations, we refer to literature values only for comparison, and instead estimate the population RF parameters of the STF model using optical imaging measurements obtained in our experiments (see RESULTS).

In V1, most cells in the upper layers are reported to be orientation selective (95%) (Leventhal et al. 1995). The peak (parafoveal) SF preference in macaques ranges from 1.5 cycles/° to ~6 cycles/° with a medium of 2.2 cycles/° (Foster et al. 1985). Other studies measure an average of ~3.2 cycles/° for complex cells (De Valois et al. 1982a). The half magnitude SF bandwidth ranges from 1 to 3 octaves for complex cells, with a mean of 1.7 (Foster et al. 1985). Others report a similar value of 1.5 octaves for complex cells in macaque (De Valois et al. 1982a). Typically, orientation bandwidths for complex cells are a bit higher than for simple cells (De Valois et al. 1982b), with median of 44° and mean of 79°.

Temporal properties of neurons in V1 seem to be more diverse (Foster et al. 1985). Neurons with band-pass properties are reported to have an average preferred TF of ~3.7 Hz (Foster et al. 1985), although other more recent studies report an average of 10Hz (Hawken et al. 1996). Neurons have bandwidths between 2 and 4 octaves, with an average of 2.75 octaves (Foster et al. 1985). Taken together, the evidence indicates there is a considerable variation in the average TF bandwidth in V1 neurons in macaque. Thus the temporal bandwidth is generally higher than the spatial bandwidth, leading to a sharper tuning for SFs.

Note that all these values are measured in parafoveal regions. Near or in the foveal region, RF parameters change. In particular, optimal SF preference increase profoundly: Foster et al. (1985) reports a doubling for V1. Other parameters are less affected by eccentricity.

### *Calculating the Expected Average Responses of the STF Model to Drifting Random Dots*

To be able to compute the expected response of a neural population using *Eq. A7*, we first have to define the stimulus $S(x, y, t)$. Here we are concerned with a static luminance pattern $N(x, y)$, which moves with constant speed $\mu$ along one direction of the visual field. Without loss of generality, we set the direction of movement in the $y$-direction, as other directions can be derived by simple rotation. Thus our stimulus has the form $S(x, y, t) = N(x, y + \mu t)$.

It is easy to verify that the Fourier transform of such a stimulus $S$ is computed as

$$\mathcal{F}\{\mathrm{N}(\mathrm{x}, \mathrm{y} + \mu\mathrm{t})\} = \mathcal{F}\{\mathrm{N}\}(\xi_\mathrm{x}, \xi_\mathrm{y})\,\delta(\mu\xi_\mathrm{y} - \xi_\mathrm{t}) \tag{A8}$$

where $\delta()$ is the delta-function. Thus, while the spectrum in $\xi_x$-dimension is unaffected by the movement, the power of the stimulus will be distributed along the $\xi_y$- and $\xi_t$-dimensions. Specifically, the original power spectrum of the luminance pattern $\mathcal{F}\{\mathrm{N}\}(\xi_\mathrm{x}, \xi_\mathrm{y})$ is projected on a plane, which is tilted towards the TF dimension. The tilted plane is defined by $\xi_t = \mu\xi_y$, as can be seen from *Eq. A8*. Thus, the larger the speed $\mu$ the more the plane is tilted into the TF direction. Substituting the result of *Eq. A8* into *Eq. A7* yields

$$\langle \mathrm{r_c}\rangle^2 = \int \left|\mathcal{F}\{\mathrm{N}\}(\xi_\mathrm{x}, \xi_\mathrm{y})\right|^2 \exp\left[-4\pi^2(\boldsymbol{\xi}-\boldsymbol{\rho})^\mathrm{T}\Sigma(\boldsymbol{\xi}-\boldsymbol{\rho}) - 4\pi^2\sigma_\mathrm{t}^2(\mu\xi_\mathrm{y}-\omega)^2\right]\mathrm{d}\xi_\mathrm{x},\,\mathrm{d}\xi_\mathrm{y} \tag{A9}$$

It turns out that this integral can be solved for specific luminance patterns $N(x, y)$ analytically, when a simple form of the spectrum of $N(x, y)$ is known. For instance, for white noise luminance patterns the Fourier transform $\mathcal{F}\{N\}$ is just constant and *Eq. A9* can be solved straightforwardly. When using grating stimuli, the Fourier transform becomes a delta-function at the frequency of the grating, and thus the average neural response is given by the integrand of Eq. A9 evaluated at the frequency of the grating.

In our main experiments, we used coherently moving, randomly positioned luminance dots as stimuli. In this case, the luminance pattern $N(x, y)$ is composed of randomly placed disks $D_r(x, y)$ of radius $r$ [where $D_r(x, y) = 1$ if $x^2 + y^2 \leq r$ and otherwise 0]. In practice, we used $2 \times 2$ square pixels rather than disks; we approximate these by a disk of radius 1 pixel lengths. Because luminance disks are positioned at random positions $(x_i, y_i)$, one can mathematically express the stimulus as convolution of disks $D_r(x, y)$ with randomly placed delta functions, i.e., $N(x, y) = D_r * H$ and $H(x, y) = \sum_i \delta(x_i - x, y_i - y)$. If we assume a sufficiently large number and a spatially uncorrelated placement of the delta functions, the Fourier transform of $H$ becomes constant (because the auto-correlation is a delta function). Taken together, we can approximate $\mathcal{F}\{N\}(\xi_x, \xi_y) \approx c\mathcal{F}\{D_r(x, y)\}$, meaning that the mean spectrum of the random dots is approximately proportional to the spectrum of an uniform disk. The Fourier transform of a uniform disk is well known and related to the so-called "Airy disk" in optics (Airy 1835). It turns out that one can approximate the amplitude of its spectrum by a Gaussian with width $\alpha = 0.044\frac{2\pi}{r}$:

$$\left|\mathcal{F}\{N_{rdots}\}(\xi_x, \xi_y)\right| \approx c \exp\left(\frac{-\xi_x^2 - \xi_y^2}{2\alpha^2}\right) \qquad (A10)$$

This approximation is equivalent to assuming that the random dots are not formed as disks of uniform luminance but as small circular Gaussian blobs. Since we have to scale the response to match the optical imaging recordings anyway, the proportionality constant $c$ reflecting the density of the dots, is irrelevant and set to 1.

By substituting *Eq. A10* into *Eq. A9* and solving the integral, the average response to random dots stimuli can be computed analytically. Note that the integral has to be solved for the different RF "blobs" and residual cross-term of the bidirectional neural population, as described above. We do not state the formula here because of its length but nevertheless use it for computing the average response in the RESULTS.

Taken together, we have derived formulas for predicting and calculating the average neural responses to drifting random dots for any given RF parameters and dot size.

### *Calculating the Critical Speed*

When increasing the speed, the energy of the stimulus gradually shifts from a neural population preferring orientations perpendicular to the axis of motion to the domains parallel to it. The response profile will reverse at a critical speed $\mu$, when the average responses around the perpendicular orientation equals the response around the parallel orientation. To derive an analytic expression for this critical speed, we approximate the critical point by calculating when the domains preferring perpendicular and parallel orientations respond equally.

Considering the geometry in frequency space of two orthogonal, bidirectional neural populations, at the critical speed the following relation should approximately hold

$$\langle r_c(\pi, \rho, \omega)\rangle^2 = 2\langle r_c(0, \rho, \omega)\rangle^2 \qquad (A11)$$

The weighting of two for the orientation domain parallel to the axis of movement originates from the fact that both directional components of the parallel domain are similarly activated, i.e., intersected by a tilted plane. In contrast, only one directional component of the orthogonal domain is activated when tilting the plane, as can be seen from the geometric arrangement of the RF blobs in frequency space (see Fig. 5*E*).

For the case when the aspect ratio is $\gamma = 1$, *Eq. A11* results in an quadratic equation and can be solved for the critical speed $\mu$. With the definitions $d_\rho \equiv 2\pi\rho a = \sqrt{\log 4}/k_\rho$ and $d_\omega \equiv 2\pi\omega\sigma_t = \sqrt{\log 4}/k_\omega$ (signifying the bandwidths, see *Eq. A3* and *Eq. A5*) it is

$$\mu_{RD} = \omega\left(\frac{d_\rho}{d_\omega\rho} + \frac{\rho'}{\alpha d_\omega}\right)\frac{d_\omega d_\rho \pm \sqrt{d_\rho^2(d_\omega^2 - \log 2) - (1 + \rho'^2)\log^2 2}}{d_\rho^2 + (1 + \rho'^2)\log 2} \qquad (A12)$$

using the abbreviation $\rho' \equiv \rho/(d_\rho\alpha)$. Note that for $\alpha \to \infty$ (meaning for very small dot sizes) it follows $\rho' \to 0$ and *Eq. A12* resembles the case for white noise, namely

$$\mu_w = c_\pm\frac{\omega}{\rho} \qquad (A13)$$

with proportionality constant $c_\pm = [d_\rho^2 \pm d_\rho/d_\omega\sqrt{d_\rho^2(d_\omega^2 - \log 2) - \log^2 2}]/(d_\rho^2 + \log 2)$. For physiologically realistic values, it is approximately $c_+ \approx 1.5$. Thus the critical speed is (mainly) determined by the ratio of the TF and SF preferences of a neural population, which we term the "preferred speed". We noticed that for the relatively small dot sizes in the experiments (ca. 0.12°), the linear relation *Eq. A13* approximated the relation *Eq. A12* reasonable well in the physiological relevant frequencies, and therefore $\mu_{RD} \approx c_\pm\frac{\omega}{\rho}$.

Note that we neglected the residual cross-terms of the RF in Fourier space in the derivation of the critical speed. Since these cross-terms are small when the four Gaussian blobs do not significantly overlap, the critical speed will be accurately predicted if the bandwidths are small. If the bandwidths are large, the cross-term will be more beneficial for the parallel orientation domain. Moreover, if the dot size was much bigger than the preferred frequency of RFs, but the bandwidth was still big enough so that there was a response, the assumption *Eq. A11* is not valid anymore because the RF "blobs" are considerably overlapping in a region where the bulk of the power of the stimulus is distributed (in this case the square root term of *Eq. A12* gets complex). In consequence, although useful for understanding the dependence of the RF parameters on the critical speed in the case of small bandwidths, the approximate critical speed of *Eq. A12* will tend to be inaccurate for large bandwidths. In RESULTS, we therefore numerically estimated the critical speed by searching for the zero crossing in the phase of the predicted orientation difference profiles for increasing drifting speeds (using the analytic response equation for bidirectional RFs including cross-terms).

## ACKNOWLEDGMENTS

We thank Zhong-Chao Tan for providing the data on grating responses.

## GRANTS

We are grateful for the partial financial support by the German Academic Exchange Service (M. J. Rasch), National Basic Research Program in China (973 Program 2011CBA00400; to H. D. Lu), Hundred Talent Program of the Chinese Academy of Sciences (2009–2011; to H. D. Lu), and National Eye Institute Grant EY-11744 (to A. W. Roe).

## DISCLOSURES

No conflicts of interest, financial or otherwise, are declared by the author(s).

## AUTHOR CONTRIBUTIONS

Author contributions: M.J.R., S.W., and H.D.L. conception and design of research; M.J.R. analyzed data; M.J.R., H.D.L., and A.W.R. interpreted results

of experiments; M.J.R. prepared figures; M.J.R. drafted manuscript; M.J.R., M.C., S.W., H.D.L., and A.W.R. approved final version of manuscript; M.C. and H.D.L. performed experiments; M.C., H.D.L., and A.W.R. edited and revised manuscript.

## REFERENCES


**Adelson E, Bergen J.** Spatiotemporal energy models for the perception of motion. *J Opt Soc Am A* 2*:* 284–299, 1985.

**Angelucci A, Bressloff PC.** Contribution of feedforward, lateral and feedback connections to the classical receptive field center and extra-classical receptive field surround of primate V1 neurons. *Progr Brain Res* 154: 93–120, 2006.

**Airy G.** On the diffraction of an object-glass with circular aperture. *Trans Cambridge Philos Soc* 5: 283, 1835.

**Baker T, Issa N.** Cortical maps of separable tuning properties predict population responses to complex visual stimuli. *J Neurophysiol* 94: 775–787, 2005.

**Basole A, White L, Fitzpatrick D.** Mapping multiple features in the population response of visual cortex. *Nature* 423: 986–990, 2003.

**Burr D, Ross J.** Direct evidence that speedlines influence motion mechanisms. *J Neurosci* 22: 8661–8664, 2002.

**Chen L, Heider B, Williams G, Healy F, Ramsden B, Roe A.** A chamber and artificial dura method for long-term optical imaging in the monkey. *J Neurosci Methods* 113: 41–49, 2002.

**De Valois R, Albrecht D, Thorell L.** Spatial frequency selectivity of cells in macaque visual cortex. *Vision Res* 22: 545–559, 1982a.

**De Valois R, William Yund E, Hepler N.** The orientation and direction selectivity of cells in macaque visual cortex. *Vision Res* 22: 531–544, 1982b.

**Dow B, Snyder A, Vautin R, Bauer R.** Magnification factor and receptive field size in foveal striate cortex of the monkey. *Exp Brain Res* 44: 213–228, 1981.

**Field D.** Relations between the statistics of natural images and the response properties of cortical cells. *J Opt Soc Am A* 4: 2379–2394, 1987.

**Foster K, Gaska J, Nagler M, Pollen D.** Spatial and temporal frequency selectivity of neurones in visual cortical areas V1 and V2 of the macaque monkey. *J Physiol* 365: 361–363, 1985.

**Geisler W.** Motion streaks provide a spatial code for motion direction. *Nature* 400: 65–69, 1999.

**Geisler W, Albrecht D, Crane A, Stern L.** Motion direction signals in the primary visual cortex of cat and monkey. *Vis Neurosci* 18: 501–516, 2001.

**Grzywacz N, Yuille A.** A model for the estimate of local image velocity by cells in the visual cortex. *Proc R Soc Lond B Biol Sci* 239: 129–161, 1990.

**Hawken M, Parker A.** Spatial properties of neurons in the monkey striate cortex. *Proc R Soc Lond B Biol Sci* 231: 251–288, 1987.

**Hawken M, Shapley R, Grosof D.** Temporal-frequency selectivity in monkey visual cortex. *Vis Neurosci* 13: 477–492, 1996.

**Heeger D.** Normalization of cell responses in cat striate cortex. *Vis Neurosci* 9: 181–197, 1992.

**Hubel D, Wiesel T.** Receptive fields, binocular interaction and functional architecture in the cat's visual cortex. *J Physiol* 160: 106–154, 1962.

**Jones J, Palmer L.** An evaluation of the two-dimensional Gabor filter model of simple receptive fields in cat striate cortex. *J Neurophysiol* 58: 1233–1258, 1987.

**Leventhal A, Thompson K, Liu D, Zhou Y, Ault S.** Concomitant sensitivity to orientation, direction, and color of cells in layers 2, 3, and 4 of monkey striate cortex. *J Neurosci* 15: 1808–1818, 1995.

**Levitt J, Kiper D, Movshon J.** Receptive fields and functional architecture of macaque V2. *J Neurophysiol* 71: 2517–2542, 1994.

**Lu H, Roe A.** Optical imaging of contrast response in macaque monkey V1 and V2. *Cereb Cortex* 17: 2675–2695, 2007.

**Lu H, Chen G, Roe A.** A map of motion streaks in V1 and V2. *SFN Abstract*, San Diego, CA: Society for Neuroscience, 2007.

**Lu H, Chen G, Tanigawa H, Roe A.** A motion direction map in macaque V2. *Neuron* 68: 1002–1013, 2010.

**Lu H, Chen G, Ts'o D, Roe A.** A rapid topographic mapping and eye alignment method using optical imaging in macaque visual cortex. *Neuroimage* 44: 636–646, 2009.

**Mante V, Carandini M.** Mapping of stimulus energy in primary visual cortex. *J Neurophysiol* 94*:* 788–798, 2005.

**Martinez L, Wang Q, Reid R, Pillai C, Alonso J, Sommer F, Hirsch J.** Receptive field structure varies with layer in the primary visual cortex. *Nat Neurosci* 8: 372–379, 2005.

**Movellan J.** Tutorial on Gabor filters. MPLab Tutorials, UCSD MPLab, Tech. Rep., 2005.

**Movshon J, Thompson I, Tolhurst D.** Spatial summation in the receptive fields of simple cells in the cat's striate cortex. *J Physiol* 283: 53–77, 1978.

**Ringach D, Hawken M, Shapley R.** Receptive field structure of neurons in monkey primary visual cortex revealed by stimulation with natural image sequences. *J Vis* 2: 12–24, 2002.

**Robson J.** Spatial and temporal contrast-sensitivity functions of the visual system. *J Opt Soc A* 56 1141–1142, 1966.

**Roe A, Ts'o D.** Visual topography in primate V2: multiple representation across functional stripes. *J Neurosci 15*: 368–369, 1995.

**Schwartz E.** Computational anatomy and functional architecture of striate cortex: a spatial mapping approach to perceptual coding. *Vision Res* 20: 645–669, 1980.

**Stork D, Wilson H.** Do Gabor functions provide appropriate descriptions of visual cortical receptive fields. *J Opt Soc Am A* 7: 1362–1373, 1990.

**Tootell R, Switkes E, Silverman M, Hamilton S.** Functional anatomy of macaque striate cortex. II. Retinotopic organization. *J Neurosci* 8: 1531–1568, 1988.

**Van Essen D, Newsome W, Maunsell J.** The visual field representation in striate cortex of the macaque monkey: asymmetries, anisotropies, and individual variability. *Vision Res* 24: 429–448, 1984.

**Watson A, Ahumada A.** Model of human visual-motion sensing. *J Opt Soc Am A* 2: 322–342, 1985.

**Zhang J, Rosenberg A, Mallik A, Husson T, Issa N.** The representation of complex images in spatial frequency domains of primary visual cortex. *J Neurosci* 27: 9310–9318, 2007.